

Galaxy And Mass Assembly (GAMA): The $0.013 < z < 0.1$ cosmic spectral energy distribution from $0.1 \mu\text{m}$ to 1mm

S.P. Driver,^{1,2*}†, A.S.G. Robotham,^{1,2} L. Kelvin,^{1,2} M. Alpaslan,^{1,2} I.K. Baldry,³ S.P. Bamford,⁴ S. Brough,⁵ M. Brown,⁶, A.M. Hopkins,⁵ J. Liske,⁷ J. Loveday,⁸ P. Norberg,⁹ J.A. Peacock,¹⁰ E. Andrae,¹¹ J.Bland-Hawthorn,¹² N. Bourne,⁴ E. Cameron,¹³ M. Colless,⁵ C.J. Conselice,⁴ S.M. Croom,¹² L. Dunne,¹⁴ C.S. Frenk,⁹ Alister W. Graham,¹⁵ M. Gunawardhana,¹² D.T. Hill,² D.H. Jones,⁶ K. Kuijken,¹⁶ B. Madore,¹⁷ R.C. Nichol,¹⁸ H.R. Parkinson,¹⁰ K.A. Pimbblet,⁶ S. Phillipps,¹⁹ C.C. Popescu,²⁰ M. Prescott,³ M. Seibert,¹⁷, R.G. Sharp,²¹ W.J. Sutherland,²² E.N. Taylor,¹² D. Thomas,¹⁸ R.J. Tuffs,¹¹ E. van Kampen,⁷ D. Wijesinghe,¹² S. Wilkins²³

¹ICRAR†, The University of Western Australia, 35 Stirling Highway, Crawley, WA 6009, Australia

²SUPA§, School of Physics & Astronomy, University of St Andrews, North Haugh, St Andrews, KY16 9SS, UK

³Astrophysics Research Institute, Liverpool John Moores University, Egerton Wharf, Birkenhead, CH41 1LD, UK

⁴Centre for Astronomy and Particle Theory, University of Nottingham, University Park, Nottingham NG7 2RD, UK

⁵Australian Astronomical Observatory, PO Box 296, Epping, NSW 1710, Australia

⁶School of Physics, Monash University, Clayton, Victoria 3800, Australia

⁷European Southern Observatory, Karl-Schwarzschild-Str. 2, 85748 Garching, Germany

⁸Astronomy Centre, University of Sussex, Falmer, Brighton BN1 9QH, UK

⁹Institute for Computational Cosmology, Department of Physics, Durham University, South Road, Durham DH1 3LE, UK

¹⁰SUPA, Institute for Astronomy, University of Edinburgh, Royal Observatory, Blackford Hill, Edinburgh EH9 3HJ, UK

¹¹Max Planck Institute for Nuclear Physics (MPIK), Saupfercheckweg 1, 69117 Heidelberg, Germany

¹²Sydney Institute for Astronomy, School of Physics, University of Sydney, NSW 2006, Australia

¹³School of Mathematical Sciences, Queensland University of Technology, GPO Box 2434, Brisbane 4001, QLD, Australia

¹⁴Department of Physics and Astronomy, University of Canterbury, Private Bag 4800, Christchurch 8140, New Zealand

¹⁵Centre for Astrophysics and Supercomputing, Swinburne University of Technology, Hawthorn, Victoria 3122, Australia

¹⁶Leiden University, P.O. Box 9500, 2300 RA Leiden, The Netherlands

¹⁷Observatories of the Carnegie Institution of Washington, 813 Santa Barbara Street, Pasadena, CA 91101, USA

¹⁸Institute of Cosmology and Gravitation (ICG), University of Portsmouth, Dennis Sciama Building, Portsmouth PO1 3FX, UK

¹⁹HH Wills Physics Laboratory, University of Bristol, Tyndall Avenue, Bristol, BS8 1TL, UK

²⁰Jeremiah Horrocks Institute, University of Central Lancashire, Preston PR1 2HE, UK

²¹Research School of Astronomy & Astrophysics, Mount Stromlo Observatory, Cotter Road, Western Creek, ACT 2611, Australia

²²Astronomy Unit, Queen Mary University London, Mile End Rd, London E1 4NS, UK

²³School of Physics and Astronomy, Oxford University, Keeble Road, Oxford, UK

24 August 2018

ABSTRACT

We use the GAMA I dataset combined with GALEX, SDSS and UKIDSS imaging to construct the low-redshift ($z < 0.1$) galaxy luminosity functions in FUV, NUV, *ugriz*, and *YJHK* bands from within a single well constrained volume of 3.4×10^5 (Mpc/h)³. The derived luminosity distributions are normalised to the SDSS DR7 main survey to reduce the estimated cosmic variance to the 5 per cent level. The data are used to construct the cosmic spectral energy distribution (CSED) from 0.1 to 2.1 μm free from any wavelength dependent cosmic variance for both the elliptical and non-elliptical populations. The two populations exhibit dramatically different CSEDs as expected for a predominantly old and young population respectively. Using the Driver et al. (2008) prescription for the azimuthally averaged photon escape fraction, the non-ellipticals are corrected for the impact of dust attenuation and the combined CSED constructed. The final results show that the Universe is currently generating $(1.8 \pm 0.3) \times 10^{35}$ h W Mpc⁻³ of which $(1.2 \pm 0.1) \times 10^{35}$ h W Mpc⁻³ is directly released into the inter-galactic medium and $(0.6 \pm 0.1) \times 10^{35}$ h W Mpc⁻³ is reprocessed and reradiated by dust in the far-IR. Using the GAMA data and our dust model we predict the mid and far-IR emission which agrees remarkably well with available data. We therefore provide a robust description of the pre- and post dust attenuated energy output of the nearby Universe from 0.1 μm to 0.6 mm. The largest uncertainty in this measurement lies in the mid and far-IR bands stemming from the dust attenuation correction and its currently poorly constrained dependence on environment, stellar mass, and morphology.

1 INTRODUCTION

The cosmic spectral energy distribution (CSED) describes the energy being generated within a representative volume of the Universe at some specified epoch. See for example Hill et al. (2010) for the most recent empirical measurement, or Somerville et al. (2012) for the most recent attempt to model the CSED. Analogous to the baryon budget (Fukugita, Hogan & Peebles 1998), the CSED or energy budget provides an empirical measurement of how the energy being produced in the Universe at some epoch is distributed as a function of wavelength. The CSED can be measured for a range of environments from voids to rich clusters to follow the progress of energy production as a function of local density. Furthermore, if one can measure the energy budget at all epochs one effectively constructs a direct empirical blueprint of the galaxy formation process, or at least its energy emission signature (see for example Finke, Razzaque & Dermer 2010).

The CSED is a predictable quantity given a cosmic star-formation history (CSFH; e.g., Hopkins & Beacom 2006), an assumed initial mass function (IMF; e.g., Kroupa 2002) along with any time (or other) dependencies, and a stellar population model (e.g., PEGASE.2, Fioc & Rocca-Volmerange 1997, 2001). In practice knowledge of the impact and evolution of dust and metallicity are also crucial and discrepancies between the predicted and actual CSED can be used to quantify these properties if the other quantities are considered known. The CSED summed and redshifted over all epochs must also reconcile with the sum of the resolved and unresolved extra-galactic background (e.g., Gilmore et al. 2011 and references therein) modulo some corrections for attenuation via the inter-galactic medium. It therefore represents a broadbrush consistency check as to whether many of our key observations and assumptions are correct and whether empirical datasets, often constructed in a relatively orthogonal manner, are in agreement.

Traditionally the main focus for CSED measurements in the nearby Universe is in the UV to far-IR wavelength range (Driver et al., 2008). This wavelength range is entirely dominated by starlight, either directly (FUV to near-IR), or starlight reprocessed by warm (mid-IR) or cold (far-IR) dust (see for example Popescu & Tuffs 2002 or Popescu et al. 2011). At low redshift the contribution from other sources (e.g., AGN) is believed to be negligible as is the contribution to the energy budget from outside the FUV-FIR range (see Driver et al. 2008). Note that this will not be the case at high redshift where the incidence of AGN is much higher (e.g., Richards et al. 2006), resulting in a possibly significant X-ray contribution to the high- z CSED. Note also that the Cosmic Microwave Background is not considered part of the nearby CSED as although photons are passing through the local volume, they do not originate from within it. Here we take the CSED as specifically describing the instantaneous energy production rate rather than the energy density which can be derived from the CSED integrated over all time (redshifted, k -corrected, and dust corrected appropriately).

The CSED is most readily constructed from the measurement of the galaxy luminosity function from a large scale galaxy redshift survey across a broad wavelength range. Measured luminosity functions in each band provide an independent estimate of the luminosity density at one specific

wavelength, and when combined form the overall CSED. However, one problem with this approach is that most surveys do not cover a sufficiently broad wavelength range to construct the full CSED. Instead the CSED has traditionally been constructed from a set of inhomogeneous surveys which suffer from systematic offsets at the survey wavelength boundaries. These offsets are difficult to quantify and might be physical, i.e., sample/cosmic variance (Driver & Robotham 2011), or to do with the measurement process, e.g., incompleteness issues (Cross & Driver 2002), or photometric measurement discrepancies (e.g., Graham et al. 2005, see also Fig. 25 of Hill et al. 2011). For example SDSS Petrosian data might be combined with 2MASS aperture photometry each with distinct biases in terms of flux measurements.

A discontinuity between the optical (*ugriz*) and near-IR data (*K*) was first noted by Wright (2001) which was eventually traced to a normalisation issue in the first SDSS luminosity functions. However an apparent offset was also noted between the *z* and *J* bands by Baldry & Glazebrook (2003) which remains unresolved. In Hill et al. (2010) we combined redshifts from the Millennium Galaxy Catalogue (Liske et al. 2003) with imaging data from the Sloan Digital Sky Survey (York et al. 2000) and the UK Infrared Deep Sky Survey Large Area Survey (Lawrence et al. 2007) to produce a 9 band CSED (*ugrizYJHK*) stretching from 0.3 to 2.1 μm . Although there was no obvious optical/near-IR discontinuity the statistical errors were quite large because of the small sample size. The six-degree field galaxy survey (6dFGS; Jones et al. 2006) also sampled the optical and near-IR regions (*bjrfJHK*) within a single survey (Hill et al. 2010) and again no obvious optical/near-IR discontinuity was seen (however the 6dF *r_F* band data appears anomalously low compared to other *r* band measurements).

Here we use data from the Galaxy And Mass Assembly survey (GAMA; Driver et al. 2009; 2011) to construct the CSED from FUV to near-IR wavelengths within a single and spectroscopically complete volume limited sample. The spectroscopic data were mainly obtained with the Anglo-Australian Telescope (Driver et al. 2011), while the optical and near-IR data is reprocessed SDSS and UKIDSS LAS imaging data, using matched apertures. The photometry was performed on data smoothed to the same resolution in each band (as described in Hill et al. 2011). Hence while cosmic variance may remain in the overall CSED amplitude, any wavelength dependence should be removed (modulo any dependence on the galaxy clustering signature within the GAMA volume).

In section 2 we describe the data and the construction of our multi-wavelength volume limited sample. In section 3 we describe the methodologies used to construct the luminosity functions and extract the luminosity densities in 11 bands. In section 4 we apply the methods to construct independent luminosity functions and the CSED respectively. In section 5 we consider the issue of dust attenuation which requires the isolation of the elliptical galaxies, believed to be dust free (Rowlands et al. 2012), and the construction of the elliptical (spheroid-dominated) and non-elliptical (disc-dominated) CSEDs. Correcting the disc-dominated population using the photon escape fractions given in Driver et al. (2008) enables the construction of the CSED both pre- and post attenuation. In section 6 we derive the present en-

ergy output of the Universe. This is extrapolated into the far-IR by calculating the attenuated energy and reallocating this to an appropriate far-IR dust emission spectrum (e.g., Dale & Helou 2002) prior to comparison with available far-IR data. The calibrated $z = 0$ pre- and post- attenuated CSED from 0.1 to 1000 μm are available on request.

Throughout this paper we use $H_0=100h\text{km s}^{-1}\text{Mpc}^{-1}$ and adopt $\Omega_M = 0.27$ and $\Omega_\Lambda = 0.73$ (Komatsu et al. 2011).

2 DATA SELECTION

The GAMA I database (Driver et al. 2011) comprises 11-band photometry from the GALEX satellite (FUV,NUV), reprocessed SDSS archival data (*ugriz*), reprocessed UKIDSS LAS archival data (*YJHK*), and spectroscopic information (redshifts) from the AAT and other sources to $r_{\text{pet}} < 19.4$ mag across three $4^\circ \times 12^\circ$ equatorial GAMA regions (see Driver et al. 2011 for a full description of the GAMA survey; Baldry et al. 2010 for the spectroscopic target selection, and Robotham et al. 2010 for the tiling procedure). Photometry for the *ugrizYJHK* bands is described in Hill et al. (2011) with revisions as given in Liske et al. (in prep.). Briefly all data are first convolved to a common $2''$ seeing. Cutouts are made at the location of each galaxy in the GAMA input catalogue. SExtractor is used to identify the central object and measure its Kron magnitude. SExtractor in dual object mode is then used to measure the flux in all other bands using the *r*-defined aperture. Hence we achieve *r*-defined matched aperture photometry from *u* to *K*. A complete description of the GAMA *u* to *K* photometry pipeline is provided in Hill et al. (2011) and has been shown to produce improved colour measurements over archival data in all bands. Here we use version 2 photometry (see Liske et al. in prep.) in which the uniformity of the convolved PSF across the *ugrizYJHK* data was improved, and some previously poor quality near-IR frames rejected.

Star-galaxy separation was implemented prior to the spectroscopic survey, as defined in Baldry et al. (2010), and used a combination of size and colour cuts. The additional optical-near-IR colour selection process was demonstrated to be highly effective in recovering compact galaxies with fairly minimal stellar contamination. The GALEX data is from a combination of MIS archival and proprietary data obtained by the MIS and GAMA teams. The GALEX photometry uses independent software optimised for galaxy source detection and flux measurement, and is described in detail in Seibert et al. (in prep.). The GALEX data is matched to the *r*-band defined catalogue following the method described in Robotham & Driver (2011) whereby flux is redistributed for multiple-matched objects according to the inverse of the first moment of the centroid offsets. Matches are either: unambiguous (single match, 46 per cent; no UV detection, 31 per cent), or redistributed between two (16 per cent), three (5 per cent), four (1 per cent), or more (1 per cent) objects.

The spectroscopic survey to $r_{\text{Pet}} < 19.4$ mag — which are predominantly acquired using the AAOmega prime-focus fibre-fed spectrographs on the Anglo-Australian Telescope — are complete to 97.0 per cent with no obvious spatial or other bias (see Driver et al. 2011). Redshifts for the spectra are assigned manually and a quality flag allocated. Following a calibration process to a standard quality system

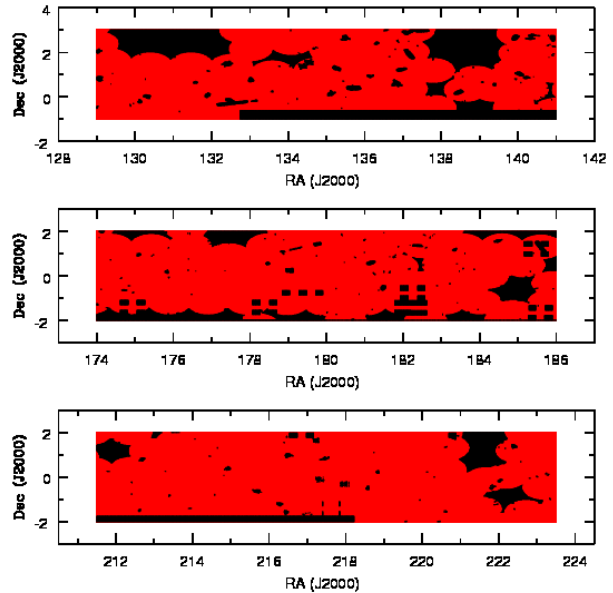


Figure 1. The area of G09 (top), G12 (centre) and G15 (bottom) surveyed in all 11 filters. The full GAMA I regions are shown in black and the common region subset in red. The total coverage is 125.06deg^2 , see Table 1 for the coverage in each band.

only $nQ \geq 3$ redshifts are used which implies a probability of being correct of > 0.9 (see Driver et al. 2011). The redshift accuracy from repeat observations is known to be $\sigma_v = \pm 65$ km/s declining to $\sigma_v = \pm 97$ km/s for the lowest signal-to-noise data (see Liske et al. in prep.).

The exact internal GAMA I catalogues extracted from the database and used for this paper are:

TilingCatv16 — cataid¹, Right Ascension, Declination, and redshift quality (see Baldry et al. 2010)

DistanceFramesv06 — flow corrected redshifts (see Baldry et al. 2012.)

ApMatchedPhotomv02 — *ugrizYJHK* Kron aperture matched photometry (see Hill et al. 2011; Liske et al. in prep.)

GalexAdvancedmatchV02 — FUV and NUV fluxes positional matching with flux redistribution (see Seibert et al. in prep.)

SersicCatv07 — *r*-band Sersic indices (see Kelvin et al. 2012.)

2.1 Extracting a common region

At the present time imaging coverage of the GAMA regions in all 11-bands is incomplete. In addition there are a number of exclusion regions where galaxies could not be detected due to bright stars and/or defects in the original SDSS imaging data. However, by far the main reason for the gaps are individual UKIDSS LAS pointings failing quality control and/or the need for GALEX to avoid very bright stars. In order to derive the 11-band CSED we must identify an area over

¹ cataid is the unique GAMA I identifier

Table 1. Coverage of the GAMA regions by filter, for a common area in all filters (All), within each GAMA sub-region (G09, G12, G15), or for the three regions combined (GAMA). Errors throughout are estimated to be $< \pm 1$ per cent.

Filter	G09 (%)	G12 (%)	G15 (%)	GAMA
FUV	83.1	89.5	93.9	88.8
NUV	84.3	90.0	93.9	89.4
u	100.0	100.0	100.0	100.0
g	100.0	100.0	100.0	100.0
r	100.0	100.0	100.0	100.0
i	100.0	100.0	100.0	100.0
z	100.0	100.0	100.0	100.0
Y	93.1	96.2	96.1	95.2
J	93.1	96.2	96.1	95.2
H	96.8	96.2	99.6	97.5
K	96.8	96.2	99.5	97.5
All	76.8	86.5	90.1	84.5

which complete photometry can be obtained, and the appropriate sky coverage of this region. Using the formula given in Driver & Robotham (2010; Eqn. 4) we find that the 1σ sample/cosmic variance in three individual GAMA pointings with $z < 0.1$ to be 14 per cent. We estimate the coverage of the complete 11-band common region by sampling our SWARPed mosaics at regular 1 arcminute intervals over the three GAMA I regions and measuring the background value at each location. A value of zero (in the case of the *ugrizYJHK* SWARPs) or a value of less than -10 (for the FUV and NUV data) indicates no data at the specified location. We then combine the 11 independent coverage maps to obtain the combined coverage map as shown in Fig. 1, and highlighting the complexity of the mask. Note that for clarity we do not include the bright star mask or SDSS exclusion mask which diminishes the area covered by a further 0.9 per cent in all bands.

The implied final survey area, which includes the common region minus masked areas, for our combined *FUVNUVugrizYJHK* catalogue is therefore 125.06 deg^2 , providing a catalogue containing 80464 objects to a uniform limit of $r_{\text{Kron}} < 19.4$ mag of which redshifts are known for 97.0 per cent (see Table 2 for completeness in other bands).

2.2 Selection limits in each band

GAMA version 2 matched aperture photometry is derived only for galaxies listed in the GAMA I input catalogue which includes multiple flux selections (see Baldry et al. 2010). This catalogue is then trimmed to a uniform spectroscopic survey limit of $r_{\text{Kron}} < 19.4$ mag. This abrupt r -band cut naturally introduces a colour bias in all other bands, making the selection limits in each band dependent on the colour distribution of the galaxy population.

To identify appropriate selection limits we show on Fig. 3 the colour magnitude diagrams for our data in each band. Following Hill et al. (2010) we identify three obvious selection boundaries for this dataset: (1) The limit at which a colour unbiased catalogue can be extracted (long dashed lines). (2) a colour dependent limit which traces the colour-bias (dotted lines). (3) a colour dependent limit until the mean colour is reached after which a constant limit is enforced (short dashed lines). Volume-corrected luminosity

distributions can be determined within each of these limits with varying pros and cons. For example while limit 1 offers the simplest and most secure route it uses the minimum amount of data increasing the random errors and susceptibility to cosmic variance. Limit 2 uses all the data but much of these data lie at very faint flux limits which are prone to large photometric error, and the shape of the boundary renders the results particularly susceptible to Eddington bias. Limit 3 represents a compromise between utilising excessive poor quality data and reducing the sample excessively. This limit was adopted in Hill et al. (2010) and we follow this practice here. The relevant limits, resulting sample sizes, and spectroscopic completeness in each band are shown on Table 2. On Fig. 2 data in the redshift range $0.013 < z < 0.1$ are shown as coloured dots.

3 METHOD

3.1 Luminosity distribution estimation

In order to derive volume-corrected luminosity distributions in each band we adopt a standard $1/V_{\text{Max}}$ method, this is preferred over a step-wise maximum likelihood method as it can better accommodate the use of multiple selection limits to overcome colour bias. The standard $1/V_{\text{Max}}$ method (Schmidt 1968) can be used to calculate the volume available to each galaxy based on its r and X magnitude limits, i.e., X_{Lim} is the brightest of $19.4 - (r - X)$ or $X_{\text{FaintLimit}}$ (where X represents FUV, NUV, *ugrizYJH* or K), and the selected redshift range (0.013 – 0.1). It is worth noting that because of the depth of the survey and the restricted redshift range that this generally constitutes a volume-limited sample at the bright-end of the recovered luminosity distribution in all bands, typically extending ~ 2 mags below L^* . Using the $1/V_{\text{Max}}$ estimator the luminosity distribution is given by:

$$\phi(M) = \frac{C_X}{\eta} \cdot \sum_{i=1}^{i=N} \left(\frac{1}{V_i}\right)$$

where the sum is over all galaxies with $M - 0.25 < M_i < M + 0.25$, η is the cosmic variance correction for the combined GAMA data over this redshift range (taken here as 0.85, see Driver et al. 2011, Fig. 20), and C_X is the inverse incompleteness given by $C_X = \frac{N(\text{all})}{N(\text{withredshifts})}$. Note that the incompleteness is handled in this simplistic way because it is so low < 3.0 per cent in all bands (see Table 2).

Our $1/V_{\text{Max}}$ estimator has been tested on trial data and the results are shown on the main panel of Fig. 3. These data were constructed using an input r -band Schechter function of $M_r^* - 5 \log_{10} h = -20.5$, $\alpha = -1.00$ and $\phi_* = 0.003$ $(\text{Mpc}/h)^{-3}$, and used to populate a 125 deg^2 volume to $z = 0.1$. Colours were allocated assuming a Gaussian colour distribution with offset $(X - r) = 3.00$ and $\sigma = 1.00$. The test sample was then truncated to $r_{\text{Kron}} < 19.4$ mag and the method described above used to recover the luminosity distribution (as indicated by the solid red data points on Fig. 3). The figure indicates that the luminosity distribution recovered is accurate (within errors) as long as > 10 galaxies are detected within a magnitude bin. It is worth highlighting that although the test data were drawn from a perfect Schechter function distribution, the transformation

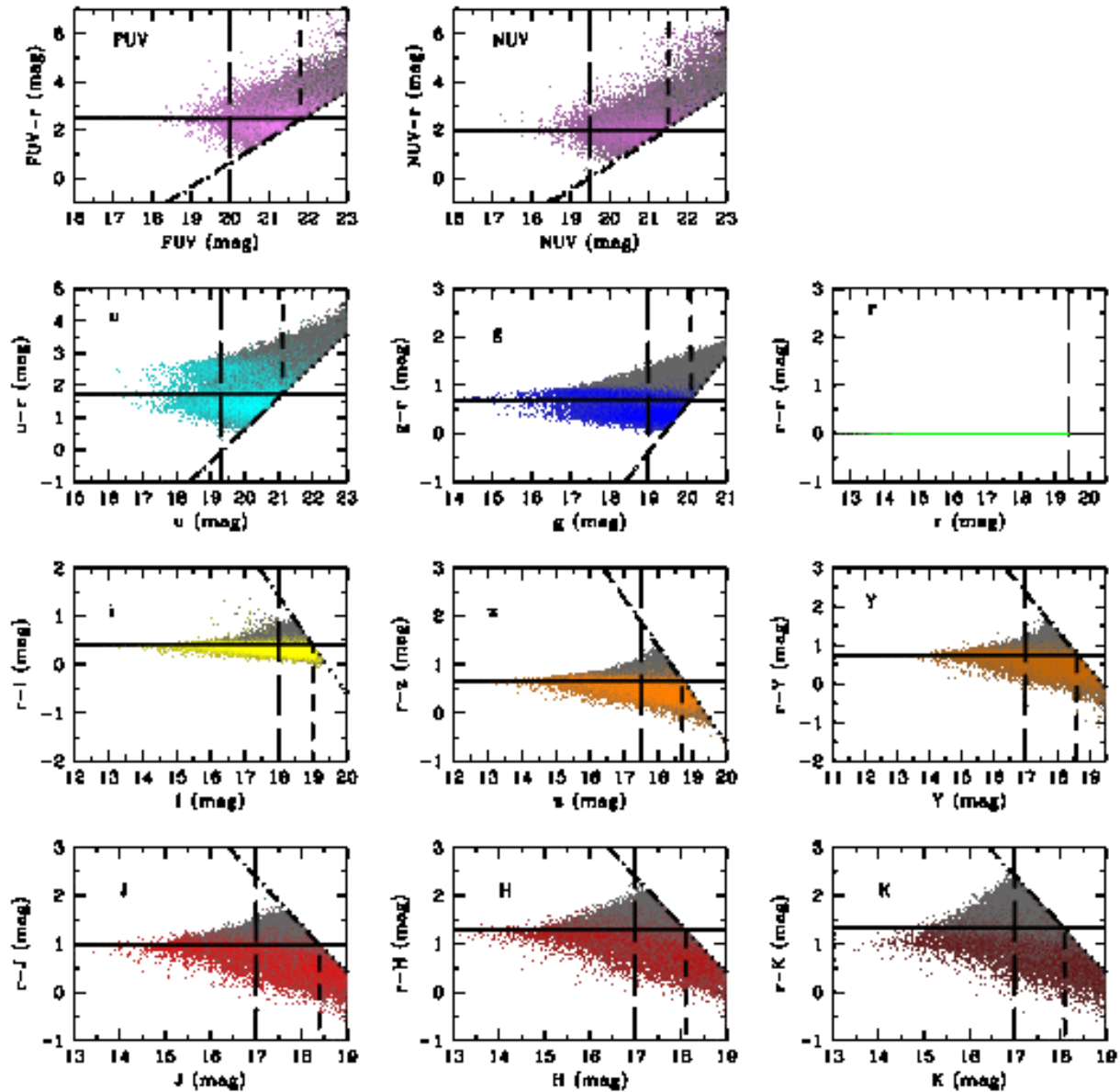


Figure 2. The colour distributions for our 11 band data w.r.t r -band. The various lines show the three selection boundaries discussed in the text with the thick medium dashed boundary taken as our final $1/V_{\text{Max}}$ limit. Data in the redshift range $0.013 < z < 0.1$ are shown in colour and these are the data used in this paper to derive the CSED.

to a second bandpass under the assumption of a Gaussian colour distribution causes the distribution to become non-Schechter like. As a consequence the bright-end of our test data, when shown in the transformed bandpass, is poorly fitted by a Schechter function (as indicated by the dotted line) with implications for the derived luminosity density as discussed in the next section. The rather obvious conclusion is that one should not expect a Schechter function to fit in all bandpasses as the colour distribution between bands essentially acts as a broad smoothing filter. This is compounded by variations in the colour distribution with

luminosity/mass and type as well as the impact of dust attenuation which will likewise smear the underlying distributions in the bluer bands (see Driver et al. 2007).

Finally we note that the method described above manages the colour bias by increasing or reducing the $1/V_{\text{Max}}$ weighting according to each objects colour. This will ultimately break-down at the low luminosity end when a galaxy of a specific colour becomes entirely undetectable at our lower redshift limit of $z \sim 0.013$. We can estimate this limit by asking what is the absolute magnitude of a galaxy with the bright limit indicated in Table 2 located at $z = 0.013$.

Table 2. Data selection process. Column 2 shows the limit above which the sample is entirely free of any colour bias. Column 3 shows the mean colour above this limit and column 4 shows the derived faint limit which we adopt in our LF analysis and is defined as the flux at which the sample becomes incomplete for the mean colour. The remaining columns show the sample size, spectroscopic completeness, and the final number of galaxies used in the luminosity function calculation once all selection limits are imposed.

Filter	Bright limit (AB mag)	Mean colour ($X - r$)	Faint limit (AB mag)	No	Comp. (%)	No ($0.013 < z < 0.1$)
FUV	20.0	2.46 ± 0.86	21.8	21740	98.2	7210
NUV	19.5	2.01 ± 0.90	21.5	30247	97.9	7989
<i>u</i>	19.3	1.73 ± 0.58	21.1	48602	97.8	10463
<i>g</i>	19.0	0.71 ± 0.27	20.1	60893	97.7	10990
<i>r</i>	19.4	N/A	19.4	80464	97.0	11032
<i>i</i>	18.0	-0.42 ± 0.09	19.0	77586	97.1	10609
<i>z</i>	17.5	-0.66 ± 0.16	18.7	72821	97.3	9756
<i>Y</i>	17.3	-0.75 ± 0.21	18.6	68156	97.5	9078
<i>J</i>	17.3	-0.98 ± 0.26	18.4	66249	97.5	8340
<i>H</i>	17.0	-1.29 ± 0.29	18.1	66428	97.5	8172
<i>K</i>	16.8	-1.33 ± 0.39	18.1	67227	97.5	7638

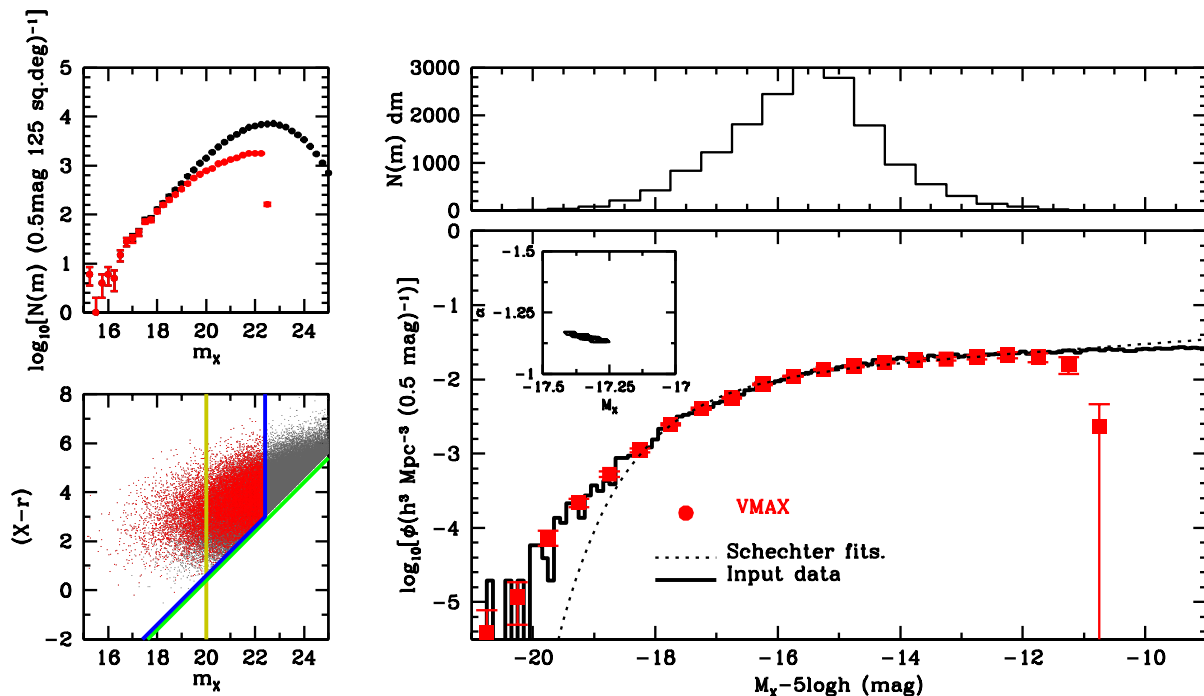


Figure 3. (*main panel*) An illustration of the accuracy of our luminosity density estimator ($1/V_{\text{MAX}}$, red squares) as compared to the input test data (solid black histogram). Also shown is the standard Schechter function fit. (*main panel inset*) The 1-, 2- and 3- σ error contours for the best fit Schechter function to the $1/V_{\text{MAX}}$ data. (*upper panel*) The actual number of galaxies used in the derivation of the luminosity distributions. (*upper left*) The galaxy number-counts prior to any flux or redshifts cuts (black data points) and after the flux and redshift cuts as indicated in Table 2. (*lower left*) The colour-magnitude diagram showing the full data set prior to cuts (black dots) and after flux and redshift cuts (coloured dots). The coloured lines denote the various selection boundaries as described in section 2.2.

These values are: -13, -13.5, -13.5, -14, -14, -15, -15.5, -15.8, -15.8, -16, and -16.2 for *FUV*, *NUV*, *ugrizYJHK* respectively and we adopt these faint absolute magnitude limits when fitting for the Schechter function parameters.

3.2 Luminosity density (j_λ)

In this paper we derive two measurements of the luminosity density. The first is from the integration of the fitted Schechter function and the second is from a direct summa-

tion of the $1/V_{\text{Max}}$ weighted fluxes. Both methods have their merits and weaknesses.

Method 1: Schechter function fitting: The $1/V_{\text{Max}}$ data is fitted by a simple three-parameter Schechter function (Schechter 1976) via standard χ^2 -minimisation. The luminosity density is then derived from the Schechter function parameters in the usual way ($j_X = \phi_X^* L_X^* \Gamma(\alpha_X + 2)$ where X denotes filter). This is perhaps the most standard way of calculating the luminosity density, but it extrapolates flux to infinitely large and small luminosities. In particular, galaxy luminosity functions often show an upturn at both bright and faint luminosities and unless more complex forms are adopted the faint-end in particular is rarely a good fit (see for example the unrestricted GAMA *ugriz* luminosity functions with a focus on the faint-end slopes reported in Loveday et al. 2012). Non-Schechter like form is often seen at the very bright-end as well, particularly in the UV and NIR wavebands (see for example Robotham & Driver 2011 or Jones et al. 2006). The errors for Method 1 are derived by mapping out the full 1-sigma error ellipse in the M^* - α plane having already optimised the normalisation at each location within this ellipse. The error is then the largest offset in M^* or α within this 1σ error ellipse.

Method 2: $1/V_{\text{Max}}$ Summation: One can directly sum the $1/V_{\text{Max}}$ weighted luminosities from the individual galaxies within the selection boundaries i.e., ($j_X = \sum_{i=0}^{i=N} 10^{-0.4(M_i - M_\odot)} / V_i$). This does not include any extrapolation but rather assumes that the galaxy luminosity distribution is fully sampled over the flux range which contributes most to the luminosity density. The errors are derived from the uncertainty in the flux measurements which we take from Hill et al. (2010) to be ± 0.03 mag in the *griz*, ± 0.05 in the *uYJHK* bands and ± 0.1 mag in the NUV and FUV (from the mag error distribution given in the GALEX-ADVANCEDMATCHV02 catalogue).

For our test data the known value is $3.0 \times 10^9 L_\odot \text{Mpc}^{-3}$ and both methods recover accurate measurements of the underlying luminosity density:

$$\begin{aligned} \text{Method 1: } & (3.03_{-0.24}^{+0.20}) \times 10^9 L_\odot \text{Mpc}^{-3}, \\ \text{Method 2: } & (2.97_{-0.18}^{+0.15}) \times 10^9 L_\odot \text{Mpc}^{-3}, \end{aligned}$$

This is perhaps surprising given the apparently poor fit of the Schechter function to the bright end of the data (Fig. 3; main panel) and indicates how strongly the integrated luminosity density depends on the L^* population. For this paper we will adopt Method 2 as our preferred luminosity density measurements for two main reasons: (1) it includes no extrapolation, and (2) it most closely mirrors the actual distribution over the region which dominates the luminosity density ($M^* \pm 2$ mag).

3.3 Cosmic energy density (ϵ)

Our luminosity densities (j_λ) are by convention quoted in units of $L_{\odot, \lambda} h \text{Mpc}^{-3}$. To convert to an energy density which represents the instantaneous energy production rate we need to multiply by the effective mean frequency of the filter in

Table 3. Various constants required for calculation of the luminosity density and energy densities.

Filter	A_λ/A_r^\dagger	λ_{Pivot} (Å)	M_\odot^\ddagger (AB mag)	p_{esc} (%)
FUV	3.045	1535	16.02	23 ± 6
NUV	3.177	2301	10.18	34 ± 6
u	1.874	3557	6.38	46 ± 6
g	1.379	4702	5.15	58 ± 6
r	1	6175	4.71	59 ± 6
i	0.758	7491	4.56	65 ± 6
z	0.538	8946	4.54	69 ± 5
Y	0.440	10305	4.52	72 ± 5
J	0.323	12354	4.57	77 ± 4
H	0.210	16458	4.71	82 ± 4
K	0.131	21603	5.19	87 ± 3

† values taken from Liske et al. (in prep.).

‡ values taken from Hill et al. (2011) for *u* to *K* and for FUV and NUV from <http://www.ucolick.org/~cnaw/sun.html>.

question (as given by the pivot wavelength, λ_p). We then convert from solar units (L_\odot) to luminosity units (WHz^{-1}). This is achieved using the formula below, where the observed energy density, ϵ^{Obs} , is given in units of $W h \text{Mpc}^{-3}$:

$$\epsilon^{\text{Obs}} = \frac{c}{\lambda} j_\lambda 10^{-0.4(M_{\odot, \lambda} - 34.10)} \quad (1)$$

the constant term of 34.10 is that required to convert AB magnitudes to luminosity units (i.e., following the Oke & Gunn 1983 definition of the AB magnitude scale in which $m_{AB} = -2.5 \log_{10} f_\nu + 56.1$, i.e., $m_{AB} = 0$ when $f_\nu = 3.631 \times 10^{-23} \text{W m}^{-2} \text{Hz}^{-1}$, and $F_\nu = 4\pi d^2 f_\nu$ where d is the standard calibration distance of 10pc). The observed energy density, ϵ^{Obs} , can be converted to an intrinsic energy density, ϵ^{Int} , using the mean photon escape fraction ($p_{\text{esc}, \lambda}$) defined in Driver et al. (2008, Fig. 3), i.e.,

$$\epsilon^{\text{Int}} = \epsilon^{\text{Obs}} / p_{\text{esc}, \lambda}. \quad (2)$$

the values adopted for the fixed parameters and their associated errors are shown in Table 3. Note that although the solar absolute magnitude is required in Eqn. 1 this is only because of the convention of reporting the luminosity density, j_λ , in units of $L_{\odot, \lambda} \text{Mpc}^{-3}$ as an intermediary step. We adopt this practice to allow for comparisons to previous work but note that the final energy densities are not dependent on the solar luminosity values used. More formally we define the luminosity density to be:

$$j_\lambda = \phi_* 10^{-0.4(M_\lambda^* - M_{\odot, \lambda})} \Gamma(\alpha + 2) \quad (3)$$

for method 1, where ϕ^* , M^* and α are the usual Schechter function parameters, and

$$j_\lambda = \sum_{n=1}^{n=i} (10^{-0.4(M_{i, \lambda} - M_\odot)} / V_{\text{Max}, i}) \quad (4)$$

for method 2, where M_i represents the absolute magnitude of the i^{th} object within the specified flux limits and $V_{\text{Max}, i}$ is the maximum volume over which this galaxy could have been seen.

4 DERIVATION OF THE LUMINOSITY DISTRIBUTIONS AND DENSITIES

4.1 Corrections to the data

Before the methodology described in the previous section can be implemented a number of corrections to the data must be made to compensate for practical issues of the observing process and known systematic effects.

4.1.1 Galactic extinction and flow corrections

The individual flux measurements in each band are Galactic extinction corrected using the Schlegel maps (Schlegel, Finkbeiner & Davis 1998) with the adopted A_v terms for the 11 bands listed in Table 3. The individual redshifts are also corrected for the local flow as described in Baldry et al. (2012). These taper the Tonry et al. (2000) multi-attractor model adopted at very low redshift ($z < 0.02$) to the CMB rest frame out to $z = 0.03$ (see also Loveday et al. 2012). This correction has no significant impact on the results in this paper but see Baldry et al. (2012) for discussions on the effect this has on the low mass end of the stellar mass function.

4.1.2 Redshift incompleteness

The redshift incompleteness for each sample is shown in Table 2. As the spectroscopic completeness is exceptionally high (> 97 per cent in all filters), it is not necessary to model the trend with magnitude, and so all results are simply scaled up by the incompleteness values. The caveat is that a highly biased incompleteness could have an impact at the very faint-end where the volumes sampled are exceptionally small. However, as we shall see the luminosity density is entirely dominated by L^* systems and small variations in the derived luminosity density at the very faint-end will have a negligible impact on the CSFD.

4.1.3 Absolute normalisation and sample/cosmic variance

In Driver et al. (2011) it was reported that the combined GAMA coverage to $z < 0.1$ is 15 per cent underdense with respect to the SDSS main survey. This was estimated by comparing the number of r-band L^* galaxies in the GAMA volume to that in the SDSS Main Survey NGP region. We therefore bootstrap to the larger SDSS area by rescaling all normalisation values upwards by 15 per cent to accommodate for this underdensity. We note that by recalibrating the L^* density to the SDSS main survey we reduce the cosmic variance in the GAMA regions from 14 per cent to the residual variance of the entire SDSS main survey which is estimated, via extrapolation, to be at the 5 per cent level, see Driver & Robotham (2010) for details.

4.1.4 k - and e - corrections

K-corrections are derived for all galaxies using the KCORRECT (v4.2) software of Blanton & Roweis (2007). We elect to use only the 9 band matched aperture photometry (i.e., SDSS and UKIDSS bands) using the appropriate SDSS and

UKIDSS bandpasses provided with the KCORRECT software. We then determine the k -corrections in all 11 bands and k -correct to redshift zero. Note that no evolutionary corrections (e -corrections) are implemented as the redshift range is low $z < 0.1$, this assumption could potentially introduce a small wavelength bias as the FUV, NUV, u and g bands will be most strongly affected by any luminosity evolution. Fig. 4 shows the k -correction for our sample. Bimodality is clear in the FUV, NUV, and u bands with values for the FUV becoming quite extreme (~ 1 mag) even at relatively low redshift ($z \sim 0.1$).

4.2 Global luminosity distributions and densities

The methods of the previous section are now applied to the data resulting in the output shown in Table 4. In all cases the data are well behaved and an acceptable goodness of fit for the Schechter function parameters is achieved in all 11-bands. Figs. 5–7 (main panels) show our recovered luminosity distributions, using our $1/V_{\text{Max}}$ method and the bright and faint limits reported in Table 2, along with the Schechter function fit to the $1/V_{\text{Max}}$ faint-limit data. Previous results are also plotted, most notably those from the GALEX, MGC, SDSS and UKIDSS surveys. In *ugriz* we also include the recent GAMA $z < 0.1$ luminosity functions from Loveday et al. (2012) which use the full GAMA area and original SDSS *Petrosian* photometry, k - and e - shifted to $z = 0$. In comparison to this previous GAMA study we generally see good agreement, although on close examination there is a consistent offset at the bright-end with our data shifted brightwards w.r.t Loveday et al. (2012). We attribute this to the known difference between *Petrosian* and Kron photometry for objects with high Sérsic index (see for example Graham et al. 2005) which typically dominate the bright-end.

In comparison to external studies the shape of the curves are mostly consistent with previous measurements with the greatest spread seen in the u and g bands (Figs. 5, lower left and right, respectively). It is important to remember that the GAMA data are, at the bright-end drawn from a volume limited sample whereas much of the literature values are flux limited. This can have a significant impact on the fitted Schechter function parameters as while the values are unaffected the associated errors will be weighted more uniformly. As a consequence the Schechter function fits are optimised towards intermediate absolute magnitudes over purely flux limited surveys. This subtlety makes it quite tricky to compare Schechter function parameters directly. However qualitatively the data and fits shown very good agreement in all bands and over all surveys.

One feature which is distinctly noticeable is the excess (upturns) at the very faint-end, particularly in the near-IR bands. This has been previously noted in many papers and explored in more detail for the GAMA dataset in the *ugriz* bands by Loveday et al. (2012). The turn-up is most likely brought about by the very red objects at the very bright-end (i.e., elliptical systems) which essentially create a plateau shortly below L^* before the more numerous star-forming blue population with an intrinsically steeper α , starts to dominate. In all cases the figures show the $1/V_{\text{Max}}$ results (which use the limits given in Table 2 col, 4) as datapoints and the $1/V_{\text{Max}}$ Bright results (which use the bright lim-

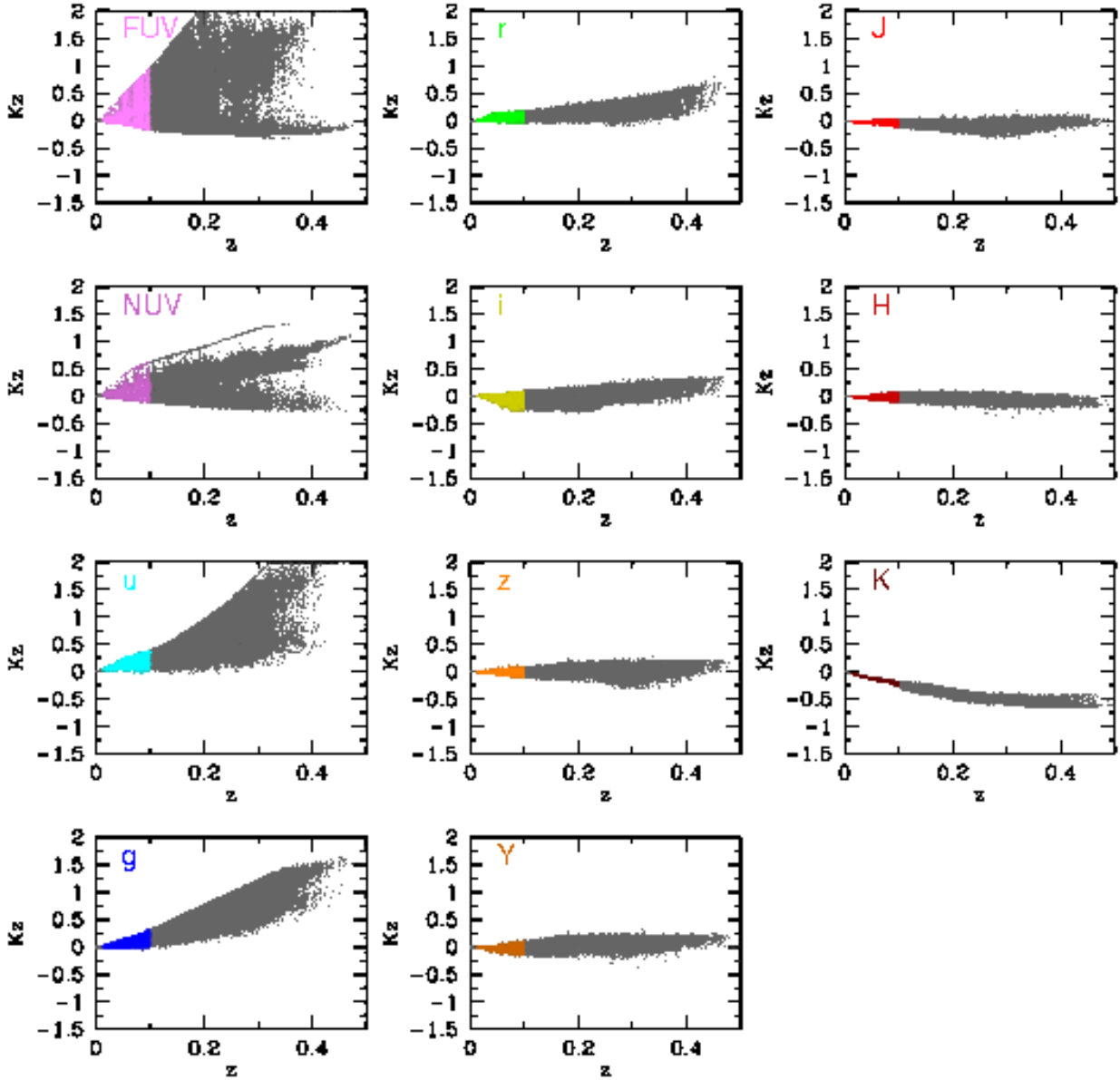


Figure 4. The k -corrections in each band for the full GAMA I sample as derived using KCORRECT (v4.2), and indicating generally well behaved distributions. Data in the redshift range $0.013 < z < 0.1$ are shown in colour and represent the data used in this paper to derive the CSED.

its given in Table 2 col, 2) as a coloured line. The best fit Schechter function (solid black line) is that fitted to the $1/V_{\text{Max}}$ data points.

From Fig. 5 to 7 the $1/V_{\text{Max}}$ and $1/V_{\text{Max}}$ -Bright results agree within the errors, as one would expect given the significant overlap in the datasets. The lower panels of Figs. 5 to 7 show the actual number of galaxies contributing to each bin (solid histogram) and the percentage contribution of each luminosity bin to the overall luminosity density (shaded histogram). The grey shading at the bright-end indicates where fewer than 10 galaxies are contributing to the recovered lu-

minosity distribution for that bin, and the grey shading at the faint-end indicates where colour bias will commence (see end of section 3.1)

In this paper we are primarily interested in the integrated luminosity density rather than the luminosity functions themselves in order to create the cosmic spectral energy distribution. In all cases we see that the main contribution to the luminosity density (see shaded histograms in lower panels of Figs. 5 to 7) stems from around L^* , with a minimal contribution from very bright and very faint systems. A key concern might be whether there exists a signif-

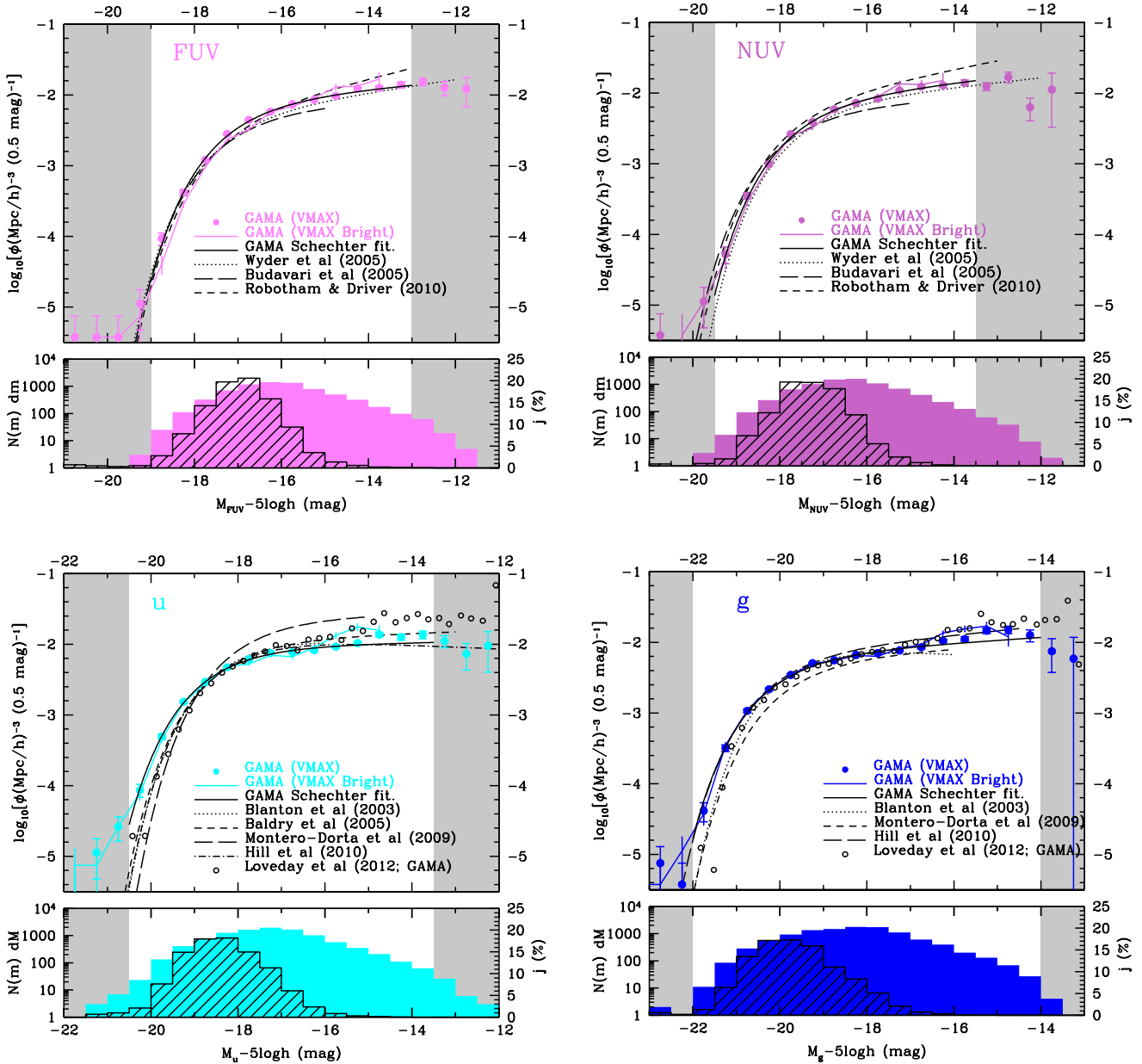


Figure 5. (*main panels*) The luminosity distribution in the FUV,NUV, u , g -bands (as indicated) derived via $1/V_{\text{MAX}}$ (solid data points) applying the corrections shown in Section 2.5. Where available, pre-existing Schechter function fits are shown. The data points with errors use the faint-limits as shown in Table 2, col. 4, whereas the line with error bars use the more conservative bright limits given in Table 2, col. 2. In all cases the faint and bright data agree within the errors. (*lower panels*) The actual number of galaxies used in the derivation of the luminosity distributions (solid histogram) and the contribution from each luminosity bin to the overall luminosity density (black shaded histogram). The grey band at the bright-end indicate as selection boundaries as described in the text.

icant contribution from any low-surface brightness systems not identified in the original SDSS imaging data. This seems unlikely as the contribution to the integrated luminosity density falls off at brighter fluxes than where surface brightness issues are expected to become significant ($M_r \sim -17$ mag). This confirms the conclusions made in Driver (1999) and Driver et al. (2006) that, while low-surface brightness galaxies may be numerous at very low luminosities, they contribute a negligible amount to the integrated luminosity densities at low redshift.

Fig. 8 shows the associated $1 - \sigma$ error ellipses for the 11 band Schechter function fits. A faint-end slope parameter of $\alpha = -1.11 \pm 0.036$ appears to be consistent with all the error ellipses although some interesting trends are seen with wavelength. These trends could be random but could also represent some faint-end incompleteness in the u and K bands. However one has to be careful as one typically moves away from the selection filter (r) one samples a narrower range in absolute magnitude and less into the faint-end up-turn which not doubt influences the values of α . However,

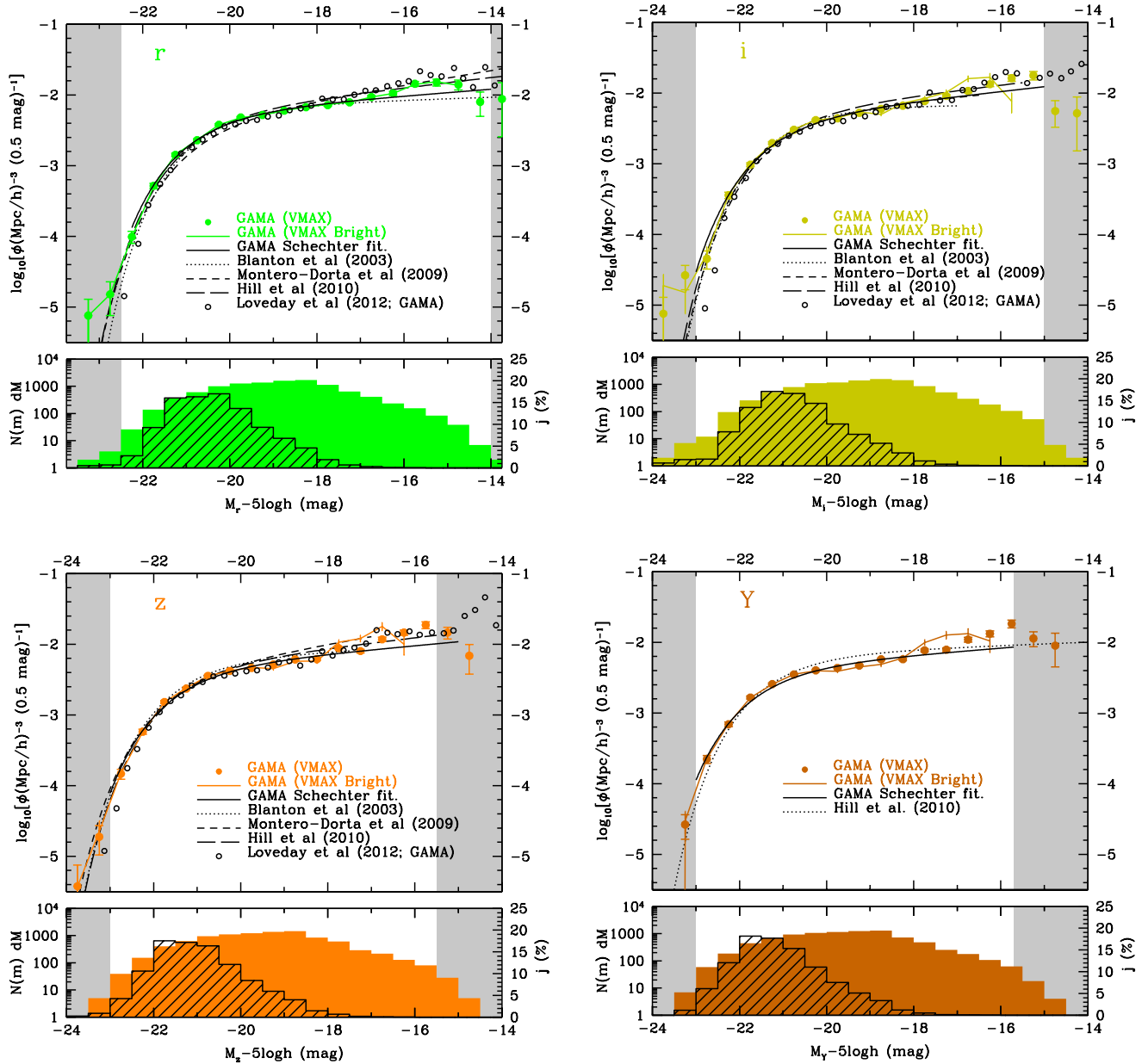
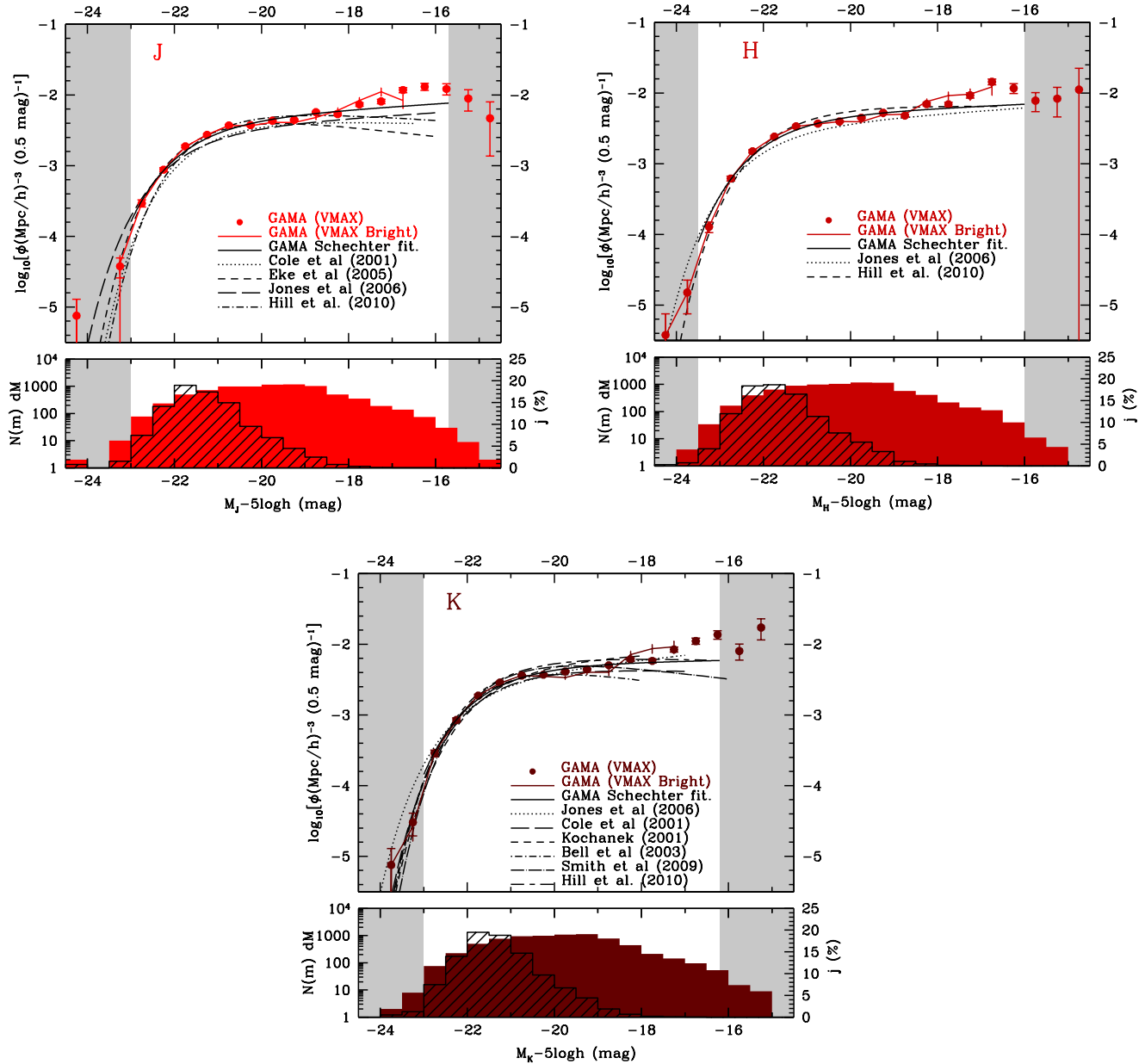


Figure 6. As for Fig. 5 but in the *rizY*-bands.

even at its steepest the relatively flat slope of $\alpha = -1.11$ implies that relatively little flux density lies outside the fitted range (as indicated by the shaded histograms in Figs. 5 — 7) and that our luminosity density estimates should be robust.

As described in Section 3 the luminosity density is measured in two ways and both of these measurements are shown on Fig. 9 and reported in Table 4. Also shown as joined black data points are the luminosity density values derived by Loveday et al. (2012) which agree extremely well as one would expect. Note that these data are shown offset in wavelength as the values were derived for filters *k*-corrected to $z = 0.1$. Reassuringly the two measurements from the distinct methods agree within their quoted errors in all 11-bands implying that there is no significant error in compar-

ing data derived via alternative methods. This is because the luminosity distributions are well sampled around the ‘knee’ and exhibit relatively modest slopes implying little contribution to the luminosity density in all bands from the low luminosity population (as discussed above). Although we have made the case that the contribution to the luminosity density is well bounded we acknowledge that the principle caveat to our values is the accuracy and completeness of the input catalogue which can only be definitively established via comparison to deeper data. As the GAMA regions will shortly be surveyed by both VST and VISTA as part of the KIDS and VIKING ESO Public Survey Programs and we defer a detailed discussion of the possible effects of incompleteness and photometric error to a future study.

Figure 7. As for Fig. 5 but in the *JHK*-bands.

4.3 The observed GAMA CSED

We now adopt the luminosity density derived from summation of the individual $1/V_{\text{MAX}}$ weights for each galaxy, i.e., Method 2. In Fig. 10 we compare these data to previous studies, most notably Hill et al. (2010) based on the Millennium Galaxy Catalogue showing data from *u* to *K*, Blanton et al. (2003) and Montero-Dorta et al. (2009) which show results from the SDSS from *u* to *z*, Jones et al. (2006) in *b_{JRFJK}*, and Wynder et al. (2005) and Robotham & Driver (2011) in the FUV and NUV. Other typically older datasets are also shown as indicated on the figure. Note that these data are now expressed as observed energy densities (i.e., ϵ^{Obs} , see section 3.3) in which the dependency on the solar SED is divided out, hence the change in shape from

Fig. 9 to Fig. 10. The new GAMA data agree extremely well with previous studies but show considerably reduced scatter (dotted lines) across the UV/optical and optical/NIR boundaries. The crucial improvement is that all the data are drawn from an identical volume with consistent photometry and therefore robust to wavelength dependent cosmic variance. In comparison to the previous compendium of data the GAMA CSED provides at least a factor of 5 improvement and exhibits a relatively smooth distribution.

Perhaps the most noticeable feature in our CSED is the apparent decline across the transition from the optical to near-IR regime reminiscent of the discontinuity seen in the earlier study by Baldry & Glazebrook (2003). Fig. 11 shows the GAMA CSED with the $z = 0$ model from Fig. 12 of

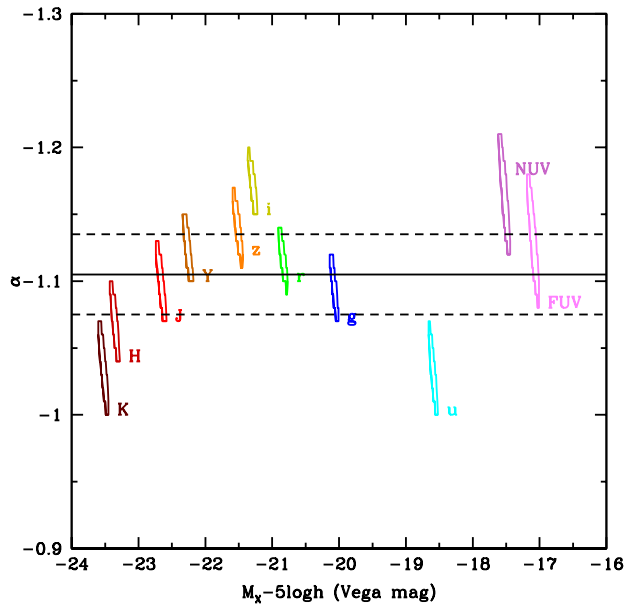


Figure 8. $1 - \sigma$ confidence ellipses for the Schechter function fits to the data shown in Figs. 5 – 7.

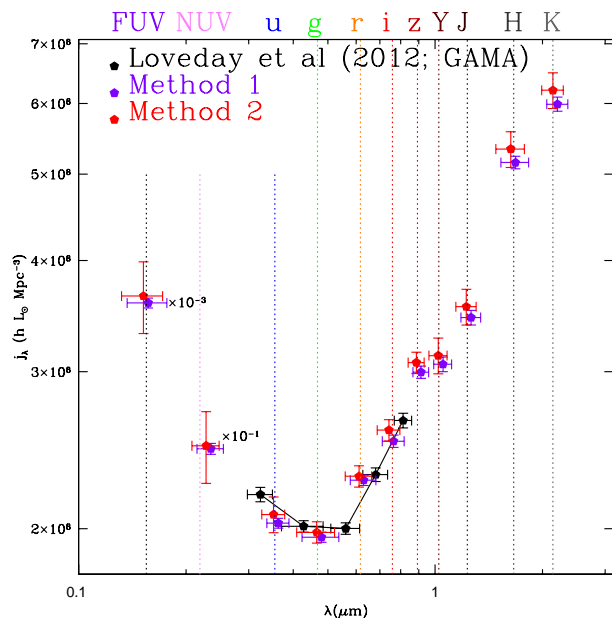


Figure 9. The luminosity density in solar units as measured through the 11 bands via the two methods. The FUV and NUV data points have been scaled as indicated. The data agree to within the errors in all cases. Method 2 is the preferred method now carried forward. Note the data have been jittered slightly in wavelength for clarity. Also shown are the values taken from Table 6 (i.e., $[\text{Col.3} + 7 \times \text{Col.4}]/8$), of Loveday et al. (2012) derived for the $^{0.1}(ugriz)$ filter set.

Somerville et al. (2012) overlaid (red line), and the same model arbitrarily scaled-up by 15 per cent (blue line). The figure highlights the apparent optical/near-IR discontinuity with the unscaled model (red line) matching the near-IR extremely well while the scaled model (blue line) matches the optical regime very well. It is difficult to understand the source of this uncertainty at this time. The two obvious possibilities are a problem with the data or a problem with the models. The GAMA CSED has been designed to minimise cosmic variance across the wavelength range by sampling an identical volume. Similarly great effort has gone into creating matched aperture photometry from u to K (Hill et al. 2011) to minimise the photometric uncertainties. It is also clear that the GAMA LFs are fully consistent with previous measurements, only a few magnitudes deeper (as indicated by the shaded regions on Figs. 5 to 7). In all cases the calculation of the luminosity density is well defined and Fig. 9 demonstrates that the precise method for measuring the CSED is not particularly critical with the data generally agreeing within the errors for both methods (which include methods which extrapolate and methods which do not). Also the GAMA CSED measurements all lie within the scatter from the compendium of individual measurements shown in Fig. 10. Moreover the Y band sits on a linear interpolation between the z and J bands. Without the Y band data one would infer a sharp discontinuity between the z and J bands, however because the Y band perfectly bridges the disjoint it suggests that the decline is a real physical phenomena.

In terms of modeling, the near-IR is not quite as simple a region as one might initially expect. Although stable low-mass stars are expected to dominate the flux, significant contribution to the NIR flux can also come from the pre-main sequence (shrouded T-Tauri stars etc) as well as the Thermally Pulsating-Asymptotic Giant Branch (TP-AGB). In particular significant attention has recently been focused on the modeling of the TP-AGB which can contribute a significant amount (~ 50 per cent) of the NIR flux for galaxies with intermediate aged stellar populations (for a detailed discussions of this topic see Maraston 2005, 2011 and Henriques et al. 2011). It is worth noting, that the model constructed in Somerville et al. (2012) does not actually include the TP-AGB and were it to be included the required offset between the red and blue curves would likely be much greater. The behaviour of the TP-AGB is also known to be strongly dependent on the metallicity with the progression through the AGB phase significantly faster for lower-metallicity stars. For exceptionally low metallicity systems the third dredge-up can be bypassed entirely, shortening the time over which a TP-AGB star might contribute significantly to the global SED. We defer a detailed discussion of this issue but note the suitability of the GAMA data for either collective or individual SED studies which extend across the optical/near-IR boundary.

5 CORRECTING FOR DUST ATTENUATION

The GAMA data shown in Fig. 10 are all drawn from an identical volume and therefore robust to cosmic variance as a function of wavelength. We therefore ascribe the variation between GAMA data and previous data, in any particular band, as most likely due to cosmic variance (and in partic-

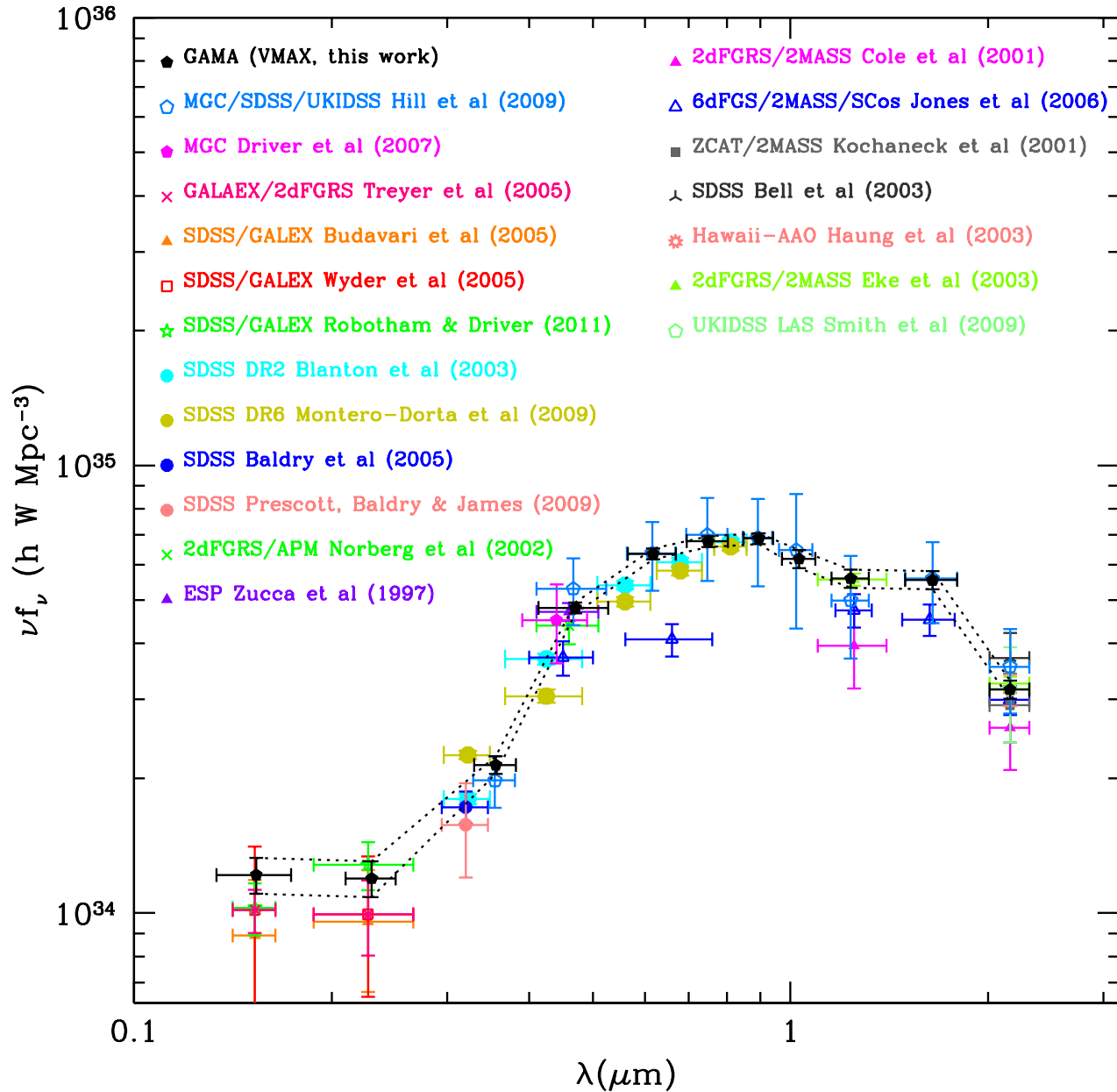


Figure 10. The *observed* cosmic spectral energy distribution from various datasets as indicated. The new GAMA data (black squares joined with dotted lines) are overlaid and the $1\text{-}\sigma$ errors connected via dotted lines which highlight the significant improvement in the uncertainty over the previous compendium of data.

ular variations in the normalisation estimates of the fitted luminosity functions). The curve and its integral represents the energy injected into the IGM by the combined nearby galaxy population, and is therefore a cosmologically interesting number. However, this energy has been attenuated by the internal dust distribution within each galaxy. In a series of earlier papers (Driver et al. 2007; 2008) we quantified the photon escape fraction for the integrated galaxy population when averaged over all viewing angles. This was achieved by deriving the galaxy luminosity function in the B band for samples of varying inclination drawn from the Millen-

nium Galaxy Catalogue (Liske et al. 2003). The observed trend of M^* with $\cos(i)$ was compared to that predicted by the sophisticated dust models of Tuffs et al. (2004, see also Popescu et al. 2011) and used to constrain the only free parameter, the face on central opacity, to $\tau_B^f = 3.8 \pm 0.7$. In Driver et al., (2008) this value was used to predict the average photon escape fraction as a function of wavelength (0.1 – 2.1 μm) and the values adopted are shown in Table 3. The errors are determined from rederiving the average photon escape fraction using the upper and lower τ_B^f values. These corrections are shown in the final column of Table 3

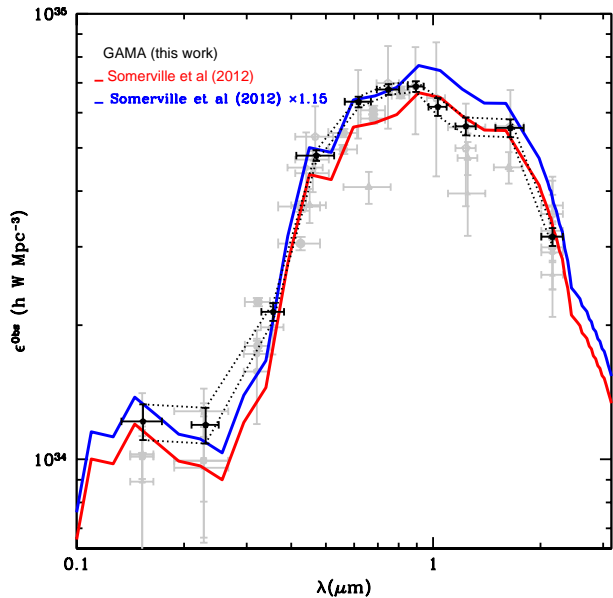


Figure 11. The *observed* cosmic spectral energy distribution from the GAMA survey with other data shown in grey. Overlaid is the model shown in Fig. 12 of Somerville et al. (2012) unscaled and scaled up by 15 per cent.

and are only applicable to the disc populations (i.e., Sabc and later).

In order to accurately correct the CSED for dust attenuation we need to isolate the elliptical population currently believed to be dust free. Rowlands et al. (2011) recently reported that less than 5% of their elliptical sample were directly detected in the far-IR Herschel-Atlas survey and when far-IR images of the remaining 95 per cent were stacked the flux recovered implied a mean dust mass of less than $10^6 M_{\odot}$. Hence while not entirely dust free this work suggests they are certainly between 100 and $1000 \times$ dust deficient when compared to similar stellar mass spiral systems. The approach we take to isolate the ellipticals is informative and therefore described in full here. Firstly we attempted to isolate the ellipticals by colour alone. Fig. 12 shows the rest-frame $(NUV - r)$ colour versus redshift in the range $0.013 < z < 0.1$ which show clear bimodality. Selecting a constant division of $(NUV - r)_{z=0} = 4.4$ mag we repeat the analysis of the previous section to derive the Schechter function parameters and luminosity distribution using our $1/V_{\text{Max}}$ method.

The derived luminosity distributions show an interesting effect in that the red population is clearly bimodal with luminosity, exhibiting faint-end upturns in most bands. Inspection of the data suggests that a simple colour cut is overly crude and a significant fraction of edge-on dusty spirals are being included in the red sample and responsible for these upturns. We conclude that colour is not a good proxy for galaxy type. In our second attempt we examine the colour-Sérsic index plane previously highlighted by Driver et al. (2005) as a better discriminator of elliptical systems than colour alone. The Sérsic indices are derived via GAMA-SIGMA (Kelvin et al. 2012, an automated wrapper for GALFIT3, Peng et al. 2010). The fitting process for the

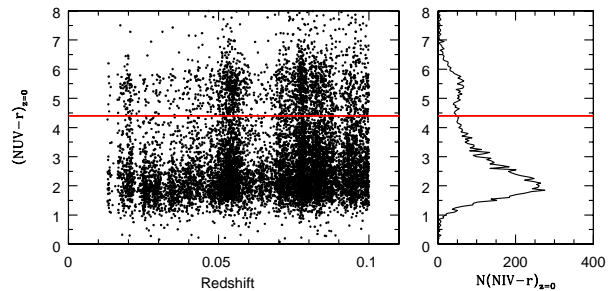


Figure 12. The rest-frame $(NUV - r)$ colour for galaxies with secure redshifts lying in the range $0.013 < z < 0.1$

GAMA sample is described in detail in Kelvin et al. (2012). Fig. 14 shows the distribution in the colour-Sérsic plane for those galaxies with secure redshifts in the range of interest ($0.013 < z < 0.1$) and flux limited to $r_{\text{Kron}} < 19.4$ mag. This sample contains 10204 galaxies and exhibits significant structure. Most noticeable are the two dense cores indicated by the two black crosses ($n = 1, (NUV - r)_{z=0} = 2$ and $n = 3.5, (NUV - r)_{z=0} = 5.5$) aligned with the anticipated locations of red elliptical and blue discs. The two populations clearly overlap and so we resort to a visual inspection of all systems with $(NUV - r) > 3.5$ mag or $n > 2$. If an object has no recorded NUV flux it is deemed red and added to the elliptical/Spheroid-dominated class.

On Fig. 14 objects classified as elliptical/Spheroid-dominated, are indicated by a red cross (1,821 systems), those eyeballed but deemed to be not elliptical as green dots (2,952), and those not inspected as grey dots (5,431). The criteria used in the visual inspection of the colour postage stamp images is that a galaxy should be concentrated, smooth, and ellipsoidal in shape with no indication of internal dust attenuation, no non-uniformity of colour, and no tidal stream/plume — all of which might be indicative of a discy (and therefore dusty) system. Eyeball classification is by definition subjective however it is clear from the distribution of the two populations that no definitive objective measure will separate the elliptical/Spheroid-dominated (henceforth spheroidal) population effectively. We do note that a Sérsic index (vertical) cut would appear to be more effective than a colour (horizontal) cut alone. This is primarily because of the colour confusion between old stellar populations in spheroidal systems and edge-on dust attenuated spirals. More complex automated strategies to morphologically classify the GAMA galaxies will be pursued in future papers once the higher quality imaging data becomes available.

We now re-derive the luminosity functions (Fig. 15) in each band for the spheroidal (red data and lines) assumed to be devoid of dust, and the remaining populations (blue lines) susceptible to intrinsic dust attenuation. Compared to Fig. 13 the bimodality in the red population is significantly less apparent suggesting that the eyeball classification is less

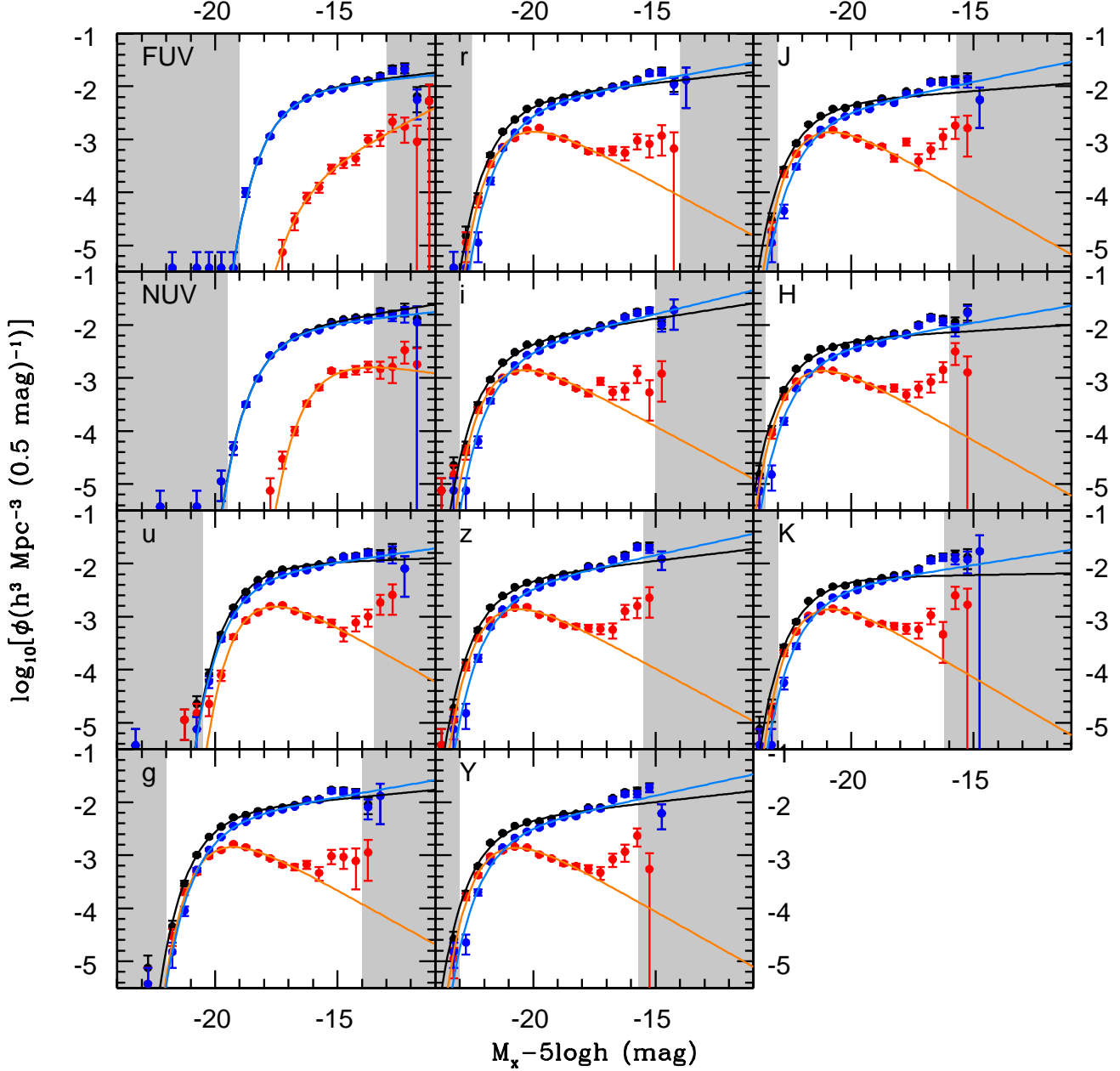


Figure 13. Total luminosity functions and those divided by colour across the 11 bands as indicated. The blue data points indicate the luminosity distributions and fitted Schechter functions for galaxies with $(NUV - r)_{z=0} < 4.4$ and the red data with galaxies with $(NUV - r) > 4.4$.

ambiguous than a simple colour cut. Tables 5 & 6 show the individual Schechter function data for the spheroidal and discy (non-spheroidal) populations respectively along with their integrated luminosity densities. We are now in a position to dust correct the spiral population and sum with the as-observed spheroidal population to provide the overall CSED corrected for dust attenuation.

6 THE ENERGY BUDGET

Table 7 and Fig. 16 show the final cosmic spectral energy distribution values from FUV through to the K band both pre- (upper) and post- (lower) dust attenuated. There are two main motivations for having constructed these data. The first is to provide an estimate of the energy production rate in the Universe today pre dust attenuation, and the second is to constrain models of galaxy formation. We defer a detailed discussion of the latter to a companion paper which introduces the two-phase galaxy formation model (Driver

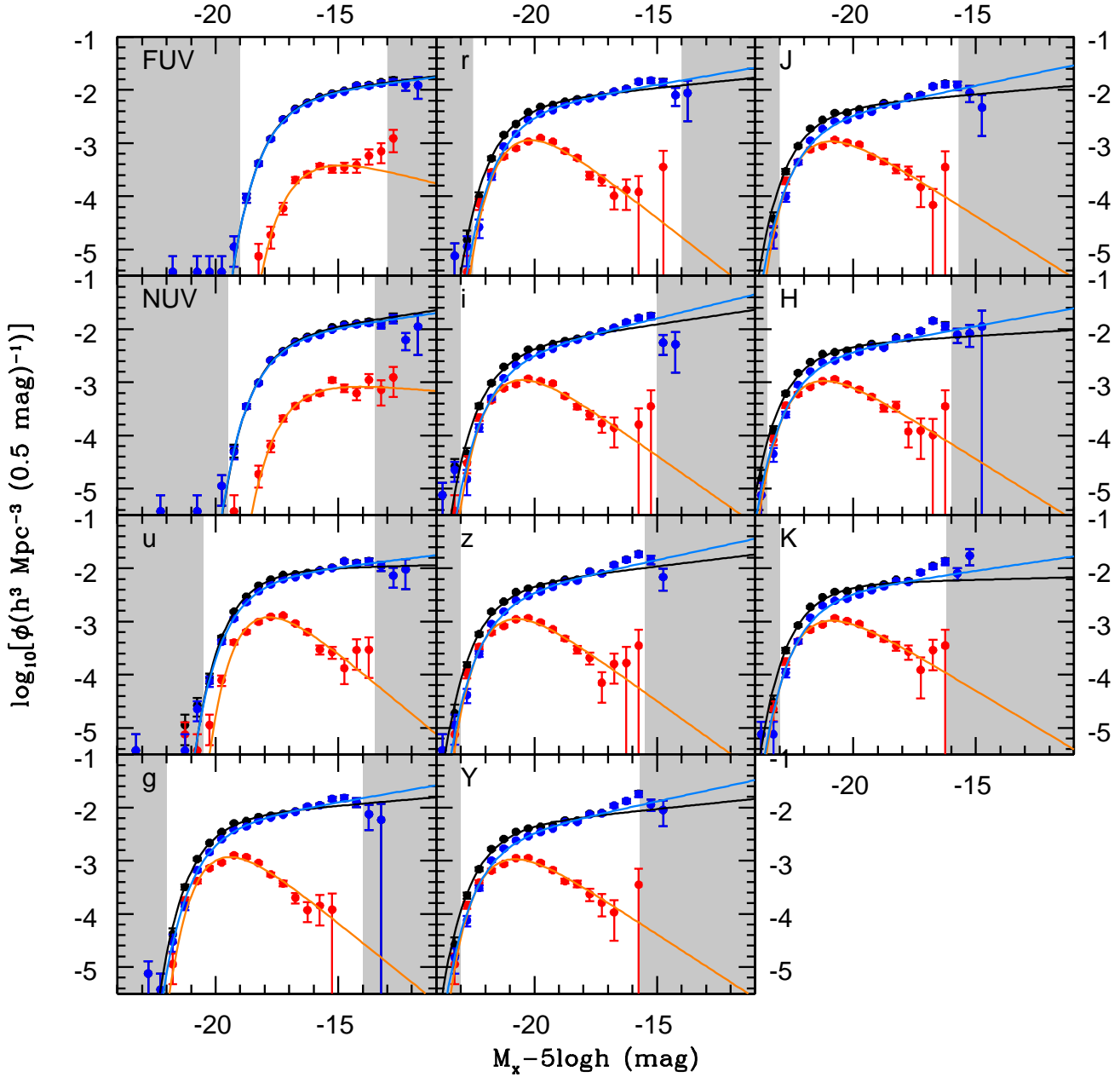


Figure 15. Total luminosity functions and those divided by eye into Spirals (blue points and lines) and ellipticals (red points and lines) across the 11 bands as indicated. The eyeball selection on a colour-Sérsic index plane is shown in Fig. 14.

et al. 2012). However before calculating the pre- and post-corrected energy density we first digress to provide an independent estimate of the the local star-formation rate from our dust-corrected FUV luminosity density.

6.1 The local star-formation rate

The dust corrected FUV luminosity density is recognised as a good proxy for the star-formation rate at the median redshift of the study concerned. This is because typically only massive stars with lifetimes less

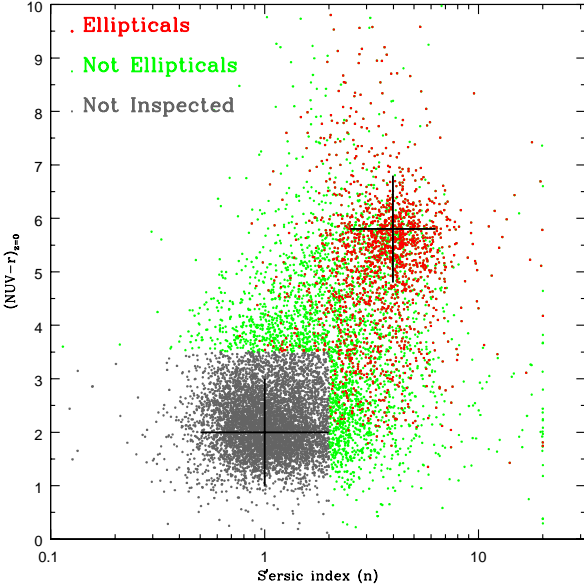
than 10Myrs contribute significant FUV flux. Following Robotham & Driver (2011) we use the standard Kennicutt (1998) prescription based on a Salpeter (1955) initial mass-function, whereby $SFR_{FUV}(M_{\odot}\text{yr}^{-1}) = 1.4 \times 10^{-28} L_{\nu}(\text{ergs s}^{-1}\text{Hz}^{-1})$ or $1.4 \times 10^{-28} \frac{\epsilon^{\text{Int}} \lambda_p}{10^{-7} \tau_c}$ to derive a star-formation rate at a volume weighted redshift of $z = 0.078$ of $0.034 \pm 0.003(\text{Random}) \pm 0.009(\text{Systematic, Dust}) \pm 0.002(\text{Systematic, cosmic variance}) \text{ h } M_{\odot} \text{ yr}^{-1} \text{ Mpc}^{-3}$. This is consistent with the compendium of results shown in Table 4 of Robotham & Driver (2011) and only ~ 9 per cent higher than the most recent values derived by Wyder et

Table 4. Luminosity function and luminosity density parameters derived for each waveband as indicated.

Filter	$M^* - 5\log h$ (AB mag)	ϕ^* ($10^{-2}h^3\text{Mpc}^{-3}$)	α	J_{Method1} ($10^8 L_{\odot} h\text{Mpc}^{-3}$)	J_{Method2} ($10^8 L_{\odot} h\text{Mpc}^{-3}$)
FUV	$-17.12^{+0.05}_{-0.03}$	$1.80^{+0.12}_{-0.07}$	$-1.14^{+0.03}_{-0.02}$	3584^{+27}_{-53}	3649^{+99}_{-102}
NUV	$-17.54^{+0.04}_{-0.03}$	$1.77^{+0.08}_{-0.08}$	$-1.17^{+0.02}_{-0.02}$	$24.6^{+0.03}_{-0.04}$	$24.8^{+0.03}_{-0.04}$
u	$-18.60^{+0.03}_{-0.03}$	$2.03^{+0.05}_{-0.08}$	$-1.03^{+0.01}_{-0.01}$	$2.03^{+0.02}_{-0.03}$	$2.08^{+0.05}_{-0.06}$
g	$-20.09^{+0.03}_{-0.03}$	$1.47^{+0.04}_{-0.04}$	$-1.10^{+0.01}_{-0.01}$	$1.96^{+0.03}_{-0.03}$	$1.98^{+0.05}_{-0.06}$
r	$-20.86^{+0.04}_{-0.02}$	$1.24^{+0.04}_{-0.03}$	$-1.12^{+0.01}_{-0.01}$	$2.27^{+0.02}_{-0.04}$	$2.29^{+0.06}_{-0.06}$
i	$-21.30^{+0.03}_{-0.03}$	$1.00^{+0.04}_{-0.03}$	$-1.17^{+0.01}_{-0.01}$	$2.51^{+0.04}_{-0.04}$	$2.58^{+0.07}_{-0.07}$
z	$-21.52^{+0.03}_{-0.04}$	$1.02^{+0.03}_{-0.03}$	$-1.14^{+0.01}_{-0.01}$	$3.00^{+0.05}_{-0.05}$	$3.07^{+0.08}_{-0.09}$
Y	$-21.63^{+0.02}_{-0.04}$	$0.98^{+0.03}_{-0.05}$	$-1.12^{+0.01}_{-0.02}$	$3.06^{+0.06}_{-0.05}$	$3.13^{+0.08}_{-0.09}$
J	$-21.74^{+0.04}_{-0.03}$	$0.97^{+0.03}_{-0.03}$	$-1.10^{+0.01}_{-0.01}$	$3.45^{+0.05}_{-0.08}$	$3.55^{+0.10}_{-0.10}$
H	$-21.99^{+0.03}_{-0.03}$	$1.03^{+0.02}_{-0.03}$	$-1.07^{+0.01}_{-0.01}$	$5.15^{+0.08}_{-0.08}$	$5.33^{+0.15}_{-0.15}$
K	$-21.63^{+0.03}_{-0.04}$	$1.10^{+0.03}_{-0.06}$	$-1.03^{+0.03}_{-0.06}$	$6.00^{+0.09}_{-0.13}$	$6.21^{+0.17}_{-0.17}$

Table 5. Luminosity function and luminosity density parameters derived for each waveband for the elliptical population as indicated.

Filter	$M^* - 5\log h$ (mag)	ϕ^* ($10^{-2}h^3\text{Mpc}^{-3}$)	α	J_{Method1} ($10^8 L_{\odot} h\text{Mpc}^{-3}$)	J_{Method2} ($10^8 L_{\odot} h\text{Mpc}^{-3}$)
FUV	$-16.20^{+0.20}_{-0.20}$	$0.16^{+0.03}_{-0.03}$	$-0.70^{+0.21}_{-0.18}$	113^{+6}_{-6}	122^{+3}_{-3}
NUV	$-16.58^{+0.12}_{-0.16}$	$0.25^{+0.04}_{-0.04}$	$-0.90^{+0.12}_{-0.11}$	$1.20^{+0.06}_{-0.06}$	$1.25^{+0.03}_{-0.03}$
u	$-17.86^{+0.06}_{-0.06}$	$0.71^{+0.02}_{-0.01}$	$-0.04^{+0.04}_{-0.06}$	$0.35^{+0.02}_{-0.01}$	$0.37^{+0.01}_{-0.01}$
g	$-19.50^{+0.06}_{-0.06}$	$0.69^{+0.01}_{-0.02}$	$-0.07^{+0.05}_{-0.04}$	$0.48^{+0.02}_{-0.02}$	$0.50^{+0.01}_{-0.01}$
r	$-20.27^{+0.06}_{-0.07}$	$0.67^{+0.02}_{-0.03}$	$-0.10^{+0.04}_{-0.05}$	$0.63^{+0.03}_{-0.03}$	$0.66^{+0.02}_{-0.02}$
i	$-20.71^{+0.06}_{-0.06}$	$0.64^{+0.01}_{-0.02}$	$-0.19^{+0.04}_{-0.04}$	$0.76^{+0.04}_{-0.02}$	$0.78^{+0.02}_{-0.02}$
z	$-20.94^{+0.06}_{-0.06}$	$0.65^{+0.01}_{-0.02}$	$-0.17^{+0.04}_{-0.04}$	$0.94^{+0.04}_{-0.04}$	$0.97^{+0.03}_{-0.03}$
Y	$-21.10^{+0.06}_{-0.06}$	$0.61^{+0.02}_{-0.02}$	$-0.25^{+0.04}_{-0.04}$	$1.00^{+0.04}_{-0.04}$	$1.02^{+0.03}_{-0.03}$
J	$-21.24^{+0.06}_{-0.05}$	$0.61^{+0.02}_{-0.02}$	$-0.27^{+0.04}_{-0.04}$	$1.17^{+0.04}_{-0.04}$	$1.18^{+0.03}_{-0.03}$
H	$-21.54^{+0.06}_{-0.05}$	$0.60^{+0.02}_{-0.01}$	$-0.28^{+0.04}_{-0.03}$	$1.74^{+0.06}_{-0.07}$	$1.76^{+0.05}_{-0.05}$
K	$-21.26^{+0.07}_{-0.06}$	$0.58^{+0.03}_{-0.01}$	$-0.31^{+0.05}_{-0.04}$	$2.02^{+0.07}_{-0.08}$	$2.03^{+0.06}_{-0.06}$

**Figure 14.** All galaxies with $n > 2$ or $(NUV - r)_{z=0} > 3.5$ have been visually inspected. Those deemed ellipticals are indicated by red crosses and those considered not elliptical as green dots. The figure indicates that Sérsic index is a better indicator of galaxy type than colour but that for any strict automated cut there is serious cross-contamination.

al. (2005) and Robotham & Driver (2011) of 0.0311 ± 0.006 and $0.0312 \pm 0.002 \text{ h M}_{\odot} \text{ yr}^{-1} \text{ Mpc}^{-3}$ respectively. Essentially all the star-formation is in the non-spheroidal systems and although formally there is $2.7 \times 10^{-4} \text{ h M}_{\odot} \text{ yr}^{-1} \text{ Mpc}^{-3}$ in the spheroid population it is highly likely that this flux might be dominated by a small number of blue spheroids (see Fig. 14).

6.2 The instantaneous energy output of the nearby Universe

Of cosmological significance is the total amount of starlight being produced in the local Universe at the present epoch and the amount which escapes into the IGM and is detectable in UV-NIR bandpasses. The discrepancy between the energy generated and that which escapes into the IGM in the optical/near-IR window, must equate to the local far-IR dust emission if starlight is the only source of heating. The implicit assumption being that the missing light is being attenuated by dust.

To evaluate the energy within the pre-attenuated CSED we must identify a suitable fitting function with which to represent the data, and will enable an extrapolation over the full UV to mid-IR regime. To do this we adopt the predicted spheroid and disc CSEDs from the zero-free parameter two-phase galaxy formation model of Driver et al. (2012) and renormalise them slightly to better fit the data. The renormalised model CSEDs are shown on Fig. 16 (lower panel) as

Table 6. Luminosity function and luminosity density parameters derived for each waveband for the non-elliptical population as indicated.

Filter	$M^* - 5\log h$ (mag)	ϕ^* ($10^{-2}h^3\text{Mpc}^{-3}$)	α	J_{Method1} ($10^8 L_{\odot} h\text{Mpc}^{-3}$)	J_{Method2} ($10^8 L_{\odot} h\text{Mpc}^{-3}$)
FUV	$-17.13^{+0.04}_{-0.05}$	$1.72^{+0.08}_{-0.09}$	$-1.14^{+0.02}_{-0.01}$	3451^{+49}_{-43}	3527^{+10}_{-10}
NUV	$-17.56^{+0.04}_{-0.04}$	$1.66^{+0.08}_{-0.08}$	$-1.16^{+0.02}_{-0.01}$	23^{+2}_{-2}	$23.5^{+0.6}_{-0.7}$
u	$-18.69^{+0.03}_{-0.04}$	$1.43^{+0.07}_{-0.07}$	$-1.14^{+0.02}_{-0.01}$	$1.68^{+0.03}_{-0.02}$	$1.70^{+0.05}_{-0.05}$
g	$-20.03^{+0.05}_{-0.02}$	$1.08^{+0.06}_{-0.03}$	$-1.20^{+0.02}_{-0.03}$	$1.48^{+0.02}_{-0.03}$	$1.48^{+0.04}_{-0.04}$
r	$-20.68^{+0.04}_{-0.02}$	$0.96^{+0.04}_{-0.02}$	$-1.20^{+0.01}_{-0.01}$	$1.61^{+0.02}_{-0.04}$	$1.63^{+0.04}_{-0.04}$
i	$-21.16^{+0.04}_{-0.04}$	$0.71^{+0.03}_{-0.03}$	$-1.28^{+0.01}_{-0.01}$	$1.75^{+0.03}_{-0.04}$	$1.80^{+0.05}_{-0.05}$
z	$-21.37^{+0.03}_{-0.04}$	$0.72^{+0.03}_{-0.04}$	$-1.25^{+0.01}_{-0.01}$	$2.05^{+0.04}_{-0.04}$	$2.10^{+0.06}_{-0.06}$
Y	$-21.54^{+0.04}_{-0.04}$	$0.63^{+0.03}_{-0.02}$	$-1.25^{+0.01}_{-0.01}$	$2.07^{+0.03}_{-0.04}$	$2.11^{+0.06}_{-0.06}$
J	$-21.67^{+0.05}_{-0.03}$	$0.60^{+0.04}_{-0.02}$	$-1.24^{+0.02}_{-0.01}$	$2.30^{+0.04}_{-0.05}$	$2.37^{+0.06}_{-0.06}$
H	$-21.92^{+0.04}_{-0.04}$	$0.65^{+0.03}_{-0.03}$	$-1.21^{+0.02}_{-0.01}$	$3.42^{+0.06}_{-0.07}$	$3.57^{+0.10}_{-0.11}$
K	$-21.55^{+0.05}_{-0.03}$	$0.70^{+0.04}_{-0.02}$	$-1.17^{+0.02}_{-0.01}$	$3.94^{+0.06}_{-0.07}$	$4.18^{+0.11}_{-0.12}$

the red and blue curve (for spheroids and discs), and provide a very good match to the data (although note once again the difficulty in matching the sharp decline in the CSED at the optical/near-IR boundary, see discussion in Section 4.3). For full details of these models see Driver et al. (2012) but in brief they adopt a distinct cosmic star-formation history for spheroids and discs, an evolving metallicity, the PEGASE star-formation code, and a Baldry & Glazebrook (2003) initial mass function.

We now integrate the models which includes extrapolation to the Lyman limit. We find a total intrinsic energy density of: $(1.8 \pm 0.3) \times 10^{35} \text{ W h Mpc}^{-3}$. This is subdivided into an energy budget of $(1.45 \pm 0.2) \times 10^{35}$ and $(0.8 \pm 0.1) \times 10^{35} \text{ W h Mpc}^{-3}$ for the non-spheroidal population before and after attenuation, and $(3.6 \pm 0.5) \times 10^{34} \text{ W h Mpc}^{-3}$ for the Spheroidal population. The final errors in the dust corrected data are almost entirely dominated by the uncertainty in the photon escape fraction (see Table 3, col 5). Our new local ($z > \sim 0.078$) energy production values (ϵ^{Int}) can be compared to our earlier estimate in Driver et al. (2008) of $\epsilon^{\text{Int}} = (1.6 \pm 0.2) \times 10^{35} \text{ W h Mpc}^{-3}$. These integrated energy values also agree within the errors to the fairly broad ranges deduced in Baldry & Glazebrook (2003) of $(1.2 - 1.7) \times 10^{35} \text{ W h Mpc}^{-3}$ for attenuated starlight of which $(0.3 - 0.7) \times 10^{35} \text{ W h Mpc}^{-3}$ is reprocessed by dust.

6.3 Predicting the local far-IR emission

The difference between the total post and pre-attenuated energies is presumed to be re-radiated in the far-IR by dust grains and equates to a total energy of $(6 \pm 1) \times 10^{34} \text{ W h Mpc}^{-3}$ at $z < 0.1$, i.e., (35 ± 3) per cent of the energy produced by stars is extracted by dust and reradiated in the far-IR (slightly lower than our previous estimate of (43 ± 5) per cent; Driver et al. 2008). Assuming that the attenuated starlight is entirely absorbed by dust and dominates over all other dust heating processes we can use this value to predict the far-IR CSED. To do this we adopt the average of the Dale & Helou (2002) models 34 and 42, following Baldry & Glazebrook (2003) and Driver et al. (2008). We then renormalise the dust emission curve until it contains the same amount of energy as that lost to the attenuation of stellar light. The attenuated starlight CSED and dust emission CSED can then be added to provide a complete

description of the CSED from the Lyman limit ($0.1 \mu\text{m}$) to the sub-mm ($< 1\text{mm}$) wavebands. This wavelength regime is crucial as it entirely dominates the energy production budget of the nearby Universe. The full $0.1\mu\text{m}$ — 1mm CSED is shown in the lower panel of Fig. 16 (black curve) and represents a prediction of the full CSED based on the GAMA UV/optical/near-IR data coupled with the photon escape fractions given in Driver et al. (2008).

On Table 8 we show how our prediction compares to the currently available data from various mid and far-IR studies. For completeness the actual values and their sources are also shown in Table 8. These data include the recent estimates in the far-IR from the Herschel-Atlas survey (Eales et al. 2009) and derived from the same dataset used by Bourne et al., (2012) in generating their Table 1. The galaxies from Bourne et al., in the redshift range $0.01 < z < 0.12$, were k- and e-corrected to redshift zero. The k- and e- corrections were derived from the stacked data and then applied to each individual galaxy prior to stacking; k-corrections were derived from the shape of the stacked SED in the redshift bin, while e-corrections were based on the evolutionary fit to luminosities in five redshift bins at $z < 0.35$, given by $L(z) \propto (1+z)^4$. Following the stacking of all optically-detected galaxies we obtain fluxes of $(5.6 \pm 0.4) \times 10^{33} \text{ WMpc}^{-3} h_{100}$ at $250 \mu\text{m}$, $(2.1 \pm 0.1) \times 10^{33} \text{ WMpc}^{-3} h_{100}$ at $350 \mu\text{m}$, and $(6.1 \pm 0.4) \times 10^{32} \text{ WMpc}^{-3} h_{100}$ at $500 \mu\text{m}$. Although these values potentially miss a small amount of faint emission the expectation is that this will be within the errors. The errors quoted include errors from the stacking process and a systematic error of 7% due to the SPIRE flux calibration uncertainty (see Pascale et al. 2012).

The match between our predicted far-IR CSED and the available data is remarkably good, and corroborate our earlier conclusion (Driver et al. 2008) that at low redshift ($z < 0.1$) the dominant source of dust heating is from attenuated starlight which is reradiated in the far-IR.

Finally in Fig. 17 we show a direct comparison of our empirically constructed CSED with that modeled by Somerville et al. (2012). In general the two curves agree within a factor of 2 with the largest discrepancies occurring in the mid and far-IR bands indicating the regions of greatest uncertainty in our understanding of the $z = 0$ energy budget. Data from the WISE mission and Herschel-Atlas

Table 7. The cosmic spectral energy distribution of the zero redshift Universe for various datasets and totals in units of h W Mpc^{-3} . The cosmic variance error is an additional ± 5 per cent affecting all datapoints in a systematic manner. The errors shown for the dust corrected data include the uncertainty in the dust correction given in Col. 5 of Table 3. Note that Col. 4 represents the luminosity density derived from the full sample not the summation of Cols. 2 & 4. However Col. 6 represents the summation of Cols. 2 & 6 and represents the final unattenuated CSED.

Wavelength	Spheroids	Discs	Total	Discs (dust corrected)	Total (dust corrected)
	$\times 10^{34} \text{ W h Mpc}^{-3}$				
FUV (0.1535)	(0.038 ± 0.003)	(1.2 ± 0.1)	(1.2 ± 0.1)	(5 ± 2)	(5 ± 2)
NUV (0.2301)	(0.058 ± 0.005)	(1.1 ± 0.1)	(1.2 ± 0.1)	(3 ± 1)	(3 ± 1)
u (0.3557)	(0.36 ± 0.02)	(1.74 ± 0.08)	(2.1 ± 0.1)	(3.8 ± 0.7)	(4.1 ± 0.8)
g (0.4702)	(1.17 ± 0.03)	(3.6 ± 0.1)	(4.7 ± 0.1)	(6.2 ± 0.9)	(7.4 ± 0.9)
r (0.6175)	(1.76 ± 0.05)	(4.5 ± 0.1)	(6.3 ± 0.2)	(7.5 ± 1.1)	(9.3 ± 1.1)
i (0.7491)	(2.00 ± 0.06)	(4.6 ± 0.1)	(6.6 ± 0.2)	(7.1 ± 0.9)	(9.0 ± 1.0)
z (0.8946)	(2.11 ± 0.06)	(4.6 ± 0.1)	(6.7 ± 0.2)	(6.6 ± 0.7)	(8.8 ± 0.8)
Y (1.0305)	(1.99 ± 0.09)	(4.1 ± 0.2)	(6.0 ± 0.3)	(5.7 ± 0.7)	(7.7 ± 0.8)
J (1.2354)	(1.84 ± 0.08)	(3.6 ± 0.2)	(5.4 ± 0.3)	(4.7 ± 0.5)	(6.5 ± 0.6)
H (1.6458)	(1.81 ± 0.08)	(3.5 ± 0.2)	(5.4 ± 0.3)	(4.3 ± 0.4)	(6.1 ± 0.5)
K (2.1603)	(1.03 ± 0.05)	(2.0 ± 0.1)	(3.0 ± 0.2)	(2.3 ± 0.2)	(3.3 ± 0.2)

[h]

Table 8. Summary of available far-IR CSED measurements at $z < 0.1$ which together with Table 7 constitute the empirical data shown on Fig. 16.

Wavelength (μm)	Dust emission $\times 10^{34} \text{ W h Mpc}^{-3}$	Facility	Reference
5.8	(1.2 ± 0.1)	Spitzer	Babbedge et al. (2006)
8	(2.6 ± 0.2)	Spitzer	Babbedge et al. (2006)
8	(1.0 ± 0.1)	Spitzer	Huang et al. (2007)
12	(0.69 ± 0.07)	PCSz/IRAS/ISO	Takeuchi et al. (2006)
25	(0.54 ± 0.05)	PCSz/IRAS/ISO	Takeuchi et al. (2006)
60	(1.6 ± 0.2)	PCSz/IRAS/ISO	Takeuchi et al. (2006)
100	(3.2 ± 0.3)	PCSz/IRAS/ISO	Takeuchi et al. (2006)
170	(2.0 ± 0.2)	PCSz/IRAS/ISO	Takeuchi et al. (2006)
250	(0.56 ± 0.04)	Herschel SPIRE	Bourne et al. (2012)
350	(0.21 ± 0.01)	Herschel SPIRE	Bourne et al. (2012)
500	(0.061 ± 0.004)	Herschel SPIRE	Bourne et al. (2012)
850	(0.0036 ± 0.0004)	PCSz/IRAS/ISO	Takeuchi et al. (2006)

(PACS) survey will be used in a follow-up paper to better constrain the CSED over these wavelength ranges.

7 CONCLUSIONS

Here we have used data from the GAMA survey (Driver et al. 2011) to provide measurements of the galaxy luminosity function in 11 bands (*FUV, NUV, ugrizYJHK*) for a low-redshift ($z < 0.1$) common imaging region. This has enabled the construction of the cosmic spectral energy distribution in unprecedented detail by producing a CSED internally robust to intrinsic cosmic variance from 0.1 to $2.2\mu\text{m}$ and absolute cosmic variance of ± 5 per cent. The results presented represent an order of magnitude improvement over measurements compiled from the literature and offer the possibility to provide significant new empirical constraints for numerical models. The data essentially confirm our previous measurement however five key results are highlighted.

1. Colour is not a good separator of spheroid-dominated and disc-dominated systems with significant contamination of the red population by edge-on discs and the existence of blue spheroids. While Sérsic index appears to be a better discriminator there is still clearly some ambiguity and no

single definitive cut. We conclude bulge-disc decomposition (e.g., Allen et al. 2007; Cameron et al. 2009) is essential to robustly disentangle the two components.

2. There appears to be a steep down-turn in the CSED at the optical/near-IR boundary which appears real and prior to *Y* band data may have given rise to the appearance of an optical/near-IR discontinuity. However that the *Y* band data sits on a linear extrapolation of the *z* to *J* band data this would imply that the rapid decline across the optical/near-IR boundary is real. Current state-of-the-art models appear to struggle to follow this decline which may imply the need for more detailed modeling of the stellar evolution assumptions in this wavelength region.

3. From our FUV data alone we derive a star-formation rate at a median redshift of $z = 0.078$ of $0.034 \pm 0.003(\text{Random}) \pm 0.009(\text{Systematic, Dust}) \pm 0.002(\text{Systematic, cosmic variance}) \text{ h M}_{\odot} \text{ yr}^{-1} \text{ Mpc}^{-3}$.

4. (35 ± 3) per cent of the energy generated by stars in the nearby Universe is attenuated by dust and reradiated in the far-IR. This value is somewhat lower than our previous estimate (45 ± 5 per cent) and although consistent within

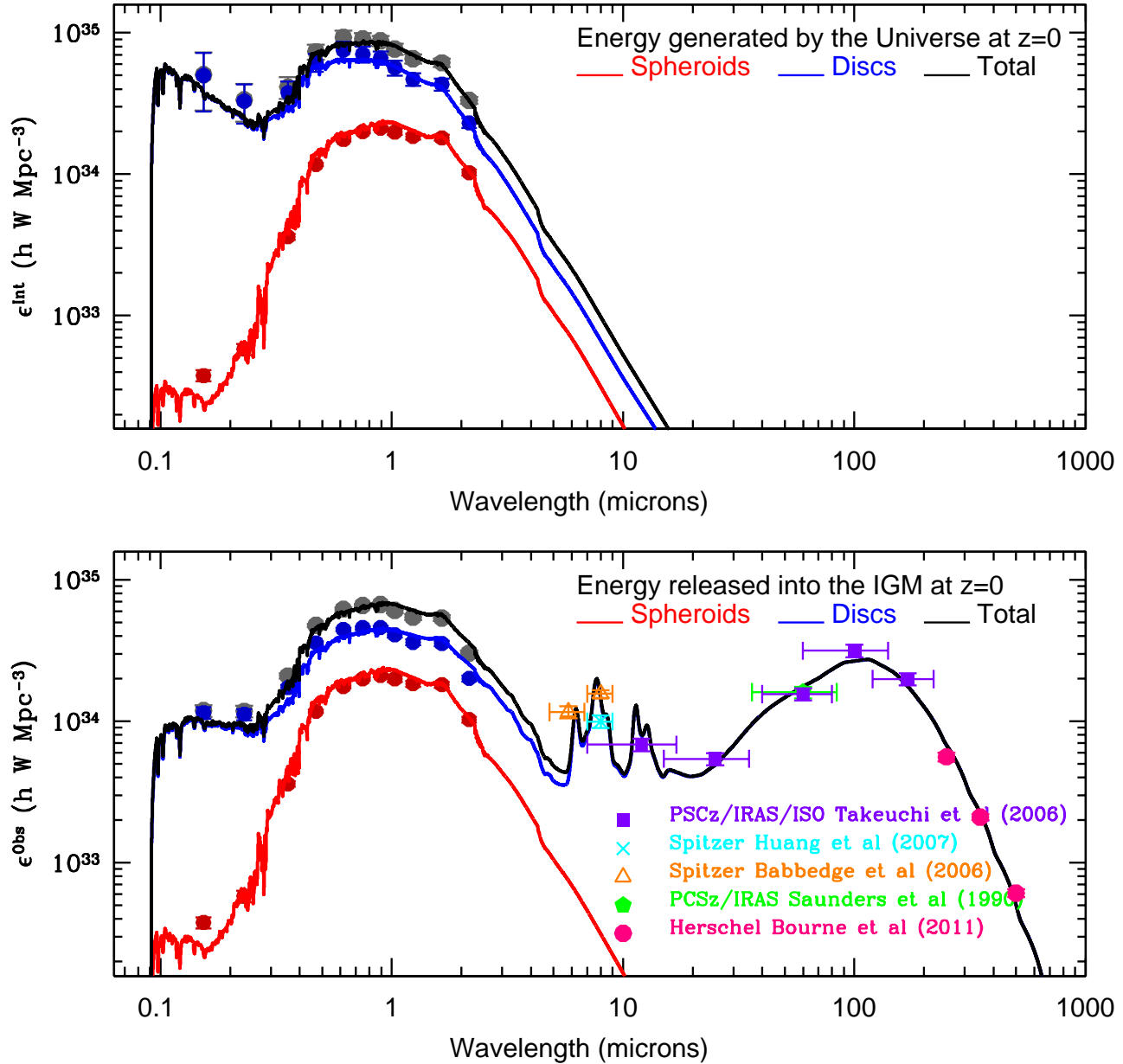


Figure 16. The energy output of the Universe from UV to FIR from spheroid dominated (red) and non-spheroid systems (blue) pre- (upper) and post- (lower) dust attenuation.

the errors the trend is mainly due to the extension of our work into the NUV and FUV bands.

5. Using the UV to near-IR CSED and the azimuthally averaged photon escape fractions we are now able to *predict* to a high degree of accuracy the complete mid-IR and far-IR energy output in the nearby Universe. The clear implication is that starlight is the dominant source of dust heating in the nearby Universe. After correcting for dust attenuation we find that the Universe is currently producing energy at a rate of $(1.8 \pm 0.3) \times 10^{35} W h Mpc^{-3}$.

In the coming years superior data from VST and VISTA along with more extensive data in the mid-IR (WISE) and far-IR (Herschel PACS) which should allow for further improvements of the CSED. Anyone wishing to obtain either our pre- or post- attenuated CSEDs should contact Simon.Driver@icrar.org.

GAMA is a joint European-Australasian project based around a spectroscopic campaign using the Anglo-Australian Telescope. The GAMA input catalogue is based on data taken from the Sloan Digital Sky Survey and the

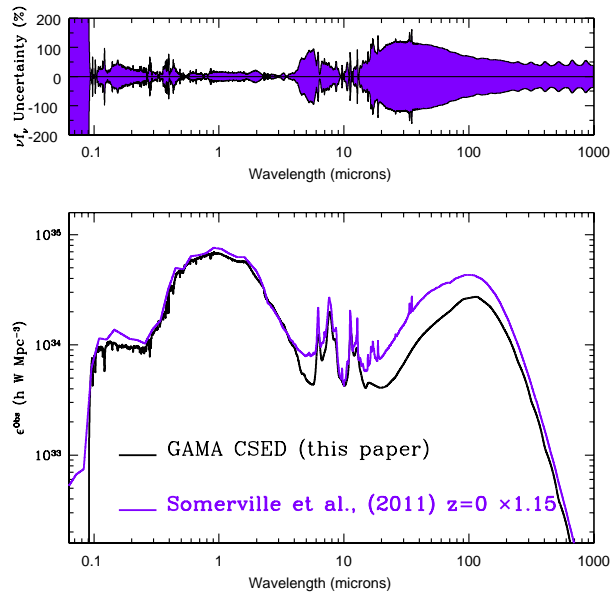


Figure 17. (main panel) A direct comparison of the Somerville et al. (2012) $z=0$ CSED and that derived in this paper. (upper panel) The ratio of the above curves indicating the wavelength regimes where there is large uncertainty in the models. The two curves have been normalised at 6175\AA (r -band).

UKIRT Infrared Deep Sky Survey. Complementary imaging of the GAMA regions is being obtained by a number of independent survey programs including GALEX MIS, VST KIDS, VISTA VIKING, WISE, Herschel-ATLAS, GMRT and ASKAP providing UV to radio coverage. GAMA is funded by the STFC (UK), the ARC (Australia), the AAO, and the participating institutions. The GAMA website is <http://www.gama-survey.org/>.

Funding for the SDSS and SDSS-II has been provided by the Alfred P. Sloan Foundation, the Participating Institutions, the National Science Foundation, the U.S. Department of Energy, the National Aeronautics and Space Administration, the Japanese Monbukagakusho, the Max Planck Society, and the Higher Education Funding Council for England. The SDSS Web Site is <http://www.sdss.org/>. The SDSS is managed by the Astrophysical Research Consortium for the Participating Institutions. The Participating Institutions are the American Museum of Natural History, Astrophysical Institute Potsdam, University of Basel, University of Cambridge, Case Western Reserve University, University of Chicago, Drexel University, Fermilab, the Institute for Advanced Study, the Japan Participation Group, Johns Hopkins University, the Joint Institute for Nuclear Astrophysics, the Kavli Institute for Particle Astrophysics and Cosmology, the Korean Scientist Group, the Chinese Academy of Sciences (LAMOST), Los Alamos National Laboratory, the Max-Planck-Institute for Astronomy (MPIA), the Max-Planck-Institute for Astrophysics (MPA), New Mexico State University, Ohio State University, University of Pittsburgh, University of Portsmouth, Princeton University, the United States Naval Observatory, and the University of Washington.

The UKIDSS project is defined in Lawrence et

al. (2007). UKIDSS uses the UKIRT Wide Field Camera (WFCAM; Casali et al 2007). The photometric system is described in Hewett et al. (2006), and the calibration is described in Hodgkin et al. (2009). The pipeline processing and science archive are described in Irwin et al. (2008) and Hambly et al. (2008). We have used data from the 4th data release.

This research has made use of the NASA/IPAC Extragalactic Database (NED), which is operated by the Jet Propulsion Laboratory, California Institute of Technology, under contract with the National Aeronautics and Space Administration.

REFERENCES

- Baldry I.K., Glazebrook K., 2003, *ApJ*, 593, 258
 Baldry I.K., et al., 2005, *MNRAS*, 358, 441
 Baldry, I.K., et al., 2010, *MNRAS*, 404, 86
 Baldry I.K., et al., 2012, *MNRAS*, 421, 621
 Bell E.F., McIntosh D.H., Katz N., Weinberg M.D., 2003, *ApJS*, 149, 289
 Bertin E., Arnouts S., 1996, *A&AS*, 117, 393
 Blanton M.R., Roweis, S., 2007, *AJ*, 113, 734
 Blanton M., et al., 2003, *ApJ*, 592, 819
 Bourne N., et al., 2012, *MNRAS*, 421, 3027
 Budavari T., et al., 2005, *ApJ*, 619, 31
 Cameron E., Driver S.P., Graham A.W., Liske J., 2009, *ApJ*, 699, 105
 Cole S. et al., 2001, *MNRAS*, 326, 255
 Cook M., Lapi A., Granato G.L., 2009, *MNRAS*, 397, 534
 Cook M., Barausse E., Evoli C., Lapi A., Granato G.L., 2010, *MNRAS*, 402, 2113
 Cook M., Evoli C., Barausse E., Granato G.L., Lapi A., 2010, *MNRAS*, 402, 941
 Cross N.J.G., Driver S.P., 2002, *MNRAS*, 329, 579
 De Propriis R., Liske J., Driver S.P., Allen P.D., Cross N.J.G., 2005, *MNRAS*, 360, 1516
 De Propriis R., Conselice C., Liske J., Driver S.P., Patton D.R., Graham A.W., Allen P.D., 2007, *ApJ*, 666, 212
 De Propriis R., et al., 2010, *AJ*, 139, 794
 Driver, S.P., Liske J., Cross N.J.G., De Propriis R., Allen P.D., 2005, *MNRAS*, 360, 81
 Driver S.P., et al., 2006, *MNRAS*, 368, 414
 Driver S.P., Popescu C.C., Tuffs R.J., Liske J., Graham A.W., Allen P.D., De Propriis, R., 2007, *MNRAS*, 379, 1022
 Driver S.P., Popescu C.C., Tuffs R.J., Graham A.W., Liske J., Baldry I., 2008, *ApJ*, 678, 101
 Driver S.P., et al., 2009, *A&G*, 50, 12
 Driver S.P., Robotham A.S.G., 2010, *MNRAS*, 407, 2131 (arXiv:1005.2538)
 Driver S.P., et al., 2011, *MNRAS*, 413, 971
 Driver S.P., et al., 2012, *MNRAS*, submitted
 Eke V.R., et al., 2004, *MNRAS*, 348, 866
 Fioc M., Rocca-Volmerange B., 1997, *A&A*, 326, 950
 Fioc M., Rocca-Volmerange B., 1999, (arXiv:9912179)
 Finke J.D., Razzaque S., Dermer C., 2010, *ApJ*, 712, 238
 Fukugita M., Hogan C.J., Peebles P.J.E., *ApJ*, 503, 518
 Gadotti D., 2009, *MNRAS*, 393, 1531
 Gallazi A., et al., 2005, *MNRAS*, 362, 41

- Gilmore R.C., Somerville R.S., Primack J.R., Dominquez A., 2012, MNRAS, 422, 3189
- Graham A.W., Driver S.P., Petrosian V., Conselice C., Ber-shady M.A., Crawford S.A., Tomotsugu G., 2005, AJ, 130, 1535
- Henriques B., Maraston C., Monaco P., Fontanot F., Menci N., De Lucia G., Tonini C., 2011, MNRAS, 415, 3571
- Hill, D., Driver S.P., Cameron E.C., Cross N.J.G., Liske J., 2010, MNRAS, 404, 1215
- Hill, D., et al., 2011, MNRAS, 412, 765
- Haung J.-S., Glazebrook K., Cowie L.L., Tinney C., 2003, ApJ, 584, 203
- Hopkins A.M., Beacom J.F., 2006, ApJ, 651, 142
- Irwin M., 2008, in ESO Astrophysics Symposium on *The 2007 ESO Instrument Calibration Workshop*, 542 (Publ: Springer)
- Jones D.H., Peterson B.A., Colless M., Saunders W., 2006, MNRAS, 369, 25
- Kelvin L. et al., 2012, MNRAS, 421, 1007
- Kennicutt, R.C. Jr., 1998, ARA&A, 36, 189
- Kochanek C., Pahre M.A., Falco E.E., Huchra J.P., Mader J., Jarrett T.H., Chester T., Cutri R., Schneider S.E., 2001, ApJ, 560, 566
- Komatsu E., et al., 2011, ApJS, 192, 18
- Kroupa P., 2002, Science, 295, 82
- Lawrence A., et al., 2007, MNRAS, 379, 1599
- Liske J., Lemon D.J., Driver S.P., Cross N.J.G., Couch W.J., 2003, MNRAS, 344, 307
- Loveday J., et al., 2012, MNRAS, 420, 1239
- Maraston C., 2005, MNRAS, 362, 799
- Maraston C., 2011, invited review (arXiv: 1104.0022)
- Möllenhoff C., Popescu C.C., Tuffs R.J., 2006, A&A, 456, 941
- Montero-Dorta A.D., Prada F., 2009, MNRAS, 399, 1106
- Nelan J.E., et al., 2005, ApJ, 632, 137
- Norberg P., et al., 2002, MNRAS, 336, 907
- Oke J.B., Gunn J.E., 1983, ApJ, 266, 713
- Pascale, E., et al., 2011, MNRAS, 415, 911
- Peng, C., Ho Luis C., Impey C.D., Rix H-W., 2010, AJ, 139, 2097
- Popescu C.C., Tuffs R.J., 2002, MNRAS, 335, 41
- Popescu C.C., Tuffs R.J., Dopita M.A., Fischera J., Kylafis N.D., Madore B.F., 2011, A&A, 527, 109
- Prescott M., Baldry I.K., James P.A., 2009, MNRAS, 397, 90
- Richards G., et al. 2006, AJ, 131, 2766
- Robotham A.S.G., et al., 2010, PASA, 27, 76
- Robotham A.S.G., Driver S.P., 2011, MNRAS, 413, 2570
- Rowlands K., et al., 2012, MNRAS, 419, 2545
- Schechter P., 1976, ApJ, 203, 297
- Schlegel D.J., Finkbeiner D.P., Davis M., 1998, ApJ, 500, 525
- Schmidt M., 1968, ApJ, 151, 393
- Smith A.J., Loveday J., Cross N.J.G., 2009, MNRAS, 397, 868
- Somerville R.S., Gilmore R.C., Primack J.R., Dominguez A., 2012, MNRAS, 423, 1992
- Tasca L.A.M., White S.D., 2011, A&A, 530, 106
- Wright E., 2001, ApJ, 556, 17
- Wyder T.K., et al., 2005, ApJ, 619, 15
- York D., et a., 2000, AJ, 120, 1579
- Zucca E. et al., 1997, A&A, 326, 477